Bar-Ilan University

Laser Cooling at Resonance

Yaakov Yudkin

Submitted in partial fulfillment of the requirements for the Master's Degree in the Department of Physics, Bar-Ilan University.

Ramat-Gan, Israel June 2018

This work was carried out under the supervision of

Prof. Lev Khaykovich

Department of Physics,
Bar-Ilan University.

Acknowledgments

I would like to express my deep and honest gratitude to my supervisor Prof. Lev Khaykovich. He is not afraid of "getting his hands dirty" in the lab or staying until late at night. Leading by example and with unlimited patience, he has taught me how to be a precise experimental physicist with enough confidence to tackle difficult and fundamental theoretical problems.

I am also grateful to the various helpful physicists at Bar-Ilan university. I would like to mention especially Prof. David A. Kessler who inspired me to conduct Monte-Carlo simulations. Without his input some of the fundamental physics would have remained uncovered. Also Prof. Eli Barkai always took special interest concerning the stochastic aspects of this work and we had many fruitful conversations.

Last, but definitely not least, I thank my loving wife Hadar. After all, she was the one who had to endure my late nights in the lab. She has always been a source of inspiration and motivation for me.

Contents

List of Figures

List of Tables

Abstract

The mechanism of Doppler cooling for a two-level atom is based on using counter-propagating, slightly red-detuned laser beams creating a preferred direction of absorption, and thus a friction force, for an atom subject to the lasers. Spontaneous emission, which naturally follows each absorption, causes the atom to conduct a random walk in momentum space and hence the velocity increases in a diffusive manner. When the (cooling) friction force and the (heating) diffusion are in equilibrium the atomic ensemble reaches a steady state temperature. This temperature, which is the main subject of the thesis, depends on how far the laser is detuned from resonance.

We show experimentally that laser cooling of lithium (^{7}Li) atoms on the D_2-line is possible when the laser light is tuned exactly to resonance with the dominant atomic transition. Since this contradicts the prediction of Doppler cooling (no preferred absorption direction and hence no cooling force) we build a more complex theoretical model to explain the phenomenon. The thesis thus comprises of two parts: one experimental and one theoretical.

In the experimental part the observation of cooling at resonance is verified. This involves determining the absolute frequency of the pump laser with high precision by carefully analyzing the fluorescence spectrum emitted by the atoms when enlightened by the pump. In addition, the laser frequency stability was enhanced to ~ 100 kHz ($\lesssim 0.02\ \Gamma$, where Γ is the line width of the excited state) by locking the laser via the current that runs the lasing diode. This scheme allows much faster frequency control than the standard piezo based technique since all mechanical elements are circumvented. All in all, the experimental error in the frequency determination is estimated $\lesssim 0.05\ \Gamma$. Also the temperature error bars are made as small as possible. For this, the temperature is first measured as a function of cooling time (duration of the optical molasses) and the steady state temperature is extracted by fitting. By making the time long enough we additionally verify that the atoms indeed reach a steady state within (typically) less than 1 ms.

Qualitatively, the phenomenon of cooling at resonance can be understood by applying simple Doppler cooling arguments to the specific hyper-fine structure of the excited state of ^{7}Li. Since it is both dense and inverted the main transition, with

respect to which the detuning is measured, is the lowest in energy and the other hyper-fine states, which remain red-detuned, are in close proximity to be populated. However, to build a good quantitative theory, which is the subject of the second part, we must resolve to a full model which takes into account both the entire atomic structure of all 24 Zeeman sub-levels and the laser light polarization ($\sigma^+ - \sigma^-$) which is dictated by the magneto-optical trap. Incorporating these features into the theory is not simple. We therefore start of by developing a few simple models ($J_g = 0 \rightarrow J_e = 1$ and $J_g = 1 \rightarrow J_e = 2$ transition) and introduce the features one-by-one. The physical phenomena appearing with each feature can thus be shown neatly. In particular, a degenerate ground state, as in the case of the $J_g = 1 \rightarrow J_e = 2$ transition and ^{7}Li, gives rise to two velocity scales. One, called the Doppler velocity v_D, is the typical velocity that becomes accessible due to Doppler cooling. The second is the capture velocity of sub-Doppler cooling v_c, a very effective cooling mechanism which arises due to a motion-induced population imbalance among the different ground states. If $v_D < v_c$ the atom will experience this additional cooling, if $v_D > v_c$ sub-Doppler cooling will fail. It is well known (experimentally) that for ^{7}Li the latter is the case and this is also verified (theoretically) by a careful analysis of the force and diffusion coefficient profiles. Here we are able to show, that the fact that the sub-Doppler cooling mechanism fails to work in ^{7}Li enhances Doppler cooling at resonance and greatly affects the steady state temperature for large and negative detuning.

Moreover, by means of Monte-Carlo simulations we show that coherent processes play an important role in showing consistency between the theory and the experimental results.

Cooling at resonance realizes a perfect combination of maximal photon scattering rate with effective cooling conditions. This can be directly applied in accurate atom counting experiments with single atom resolution which would clearly benefit from this favorable combination.

This joint experimental and theoretical work was pulbished recently in Physical Review A and was highlited as an "Editor's Suggestion" paper [1].

Chapter 1

Introduction and Motivation

The research field of cold atoms is huge [2]. Many universities and research institutions around the globe have one or multiple groups working on a variety of cold atom applications, both experimental and theoretical.

It all started four decades ago, shortly after the invention of the laser, when the idea of using on resonance radiation pressure to reduce the atomic velocity was first set forward [3, 4] and theoretically investigated [5]. Among other, a fundamental limit for the temperature, known as the Doppler limit, was predicted. A decade later the first experimental implementation, using sodium atoms, was reported on. Although it seemed at first that the theoretical prediction worked well [6], later and more precise measurements showed temperatures an order of magnitude below the Doppler limit [7]. The cold atoms community at the time greeted this discovery with enthusiasm and raced towards even lower temperatures with the goal of achieving quantum degeneracy. While this important milestone was finally achieved in the mid 90s [8, 9] the verification of the Doppler limit remains somewhat elusive. The work presented here is an important contribution to filling that hole.

As we set out to investigate Doppler cooling at resonance conditions it was not the above that we were focused on. Recent theoretical [10] and experimental [11] works have shown that non-Gaussian velocity distributions (so-called Levy statistics) are found in certain setups. We found, using the model introduced years ago [5], that a velocity distribution following a power-law should also be observed in regular Doppler cooling [12]. This is most exemplified as the laser frequency approaches resonance with the atomic transition. Although this regime is experimentally demanding we took it upon ourselves to investigate this phenomenon. As we began measurements we discovered an unexpected turn of events: The velocity distribution remained highly Gaussian not only close to resonance but even beyond. This discovery was especially surprising because, according to the decades old theory, laser cooling does not work at resonance. We thus refocused our work on understanding the "weir" phenomenon of laser cooling at resonance.

This thesis is structured as follows. In Chap. 2 the simple model involving a two-level atom in a one-dimensional (1D) laser setup is presented. This serves as a theoretical background and introduces the analytical solution for the Doppler limit. At the end of the chapter, in Sec. 2.7, some previous experiments are discussed briefly. These examples serve to show the validity and some discrepancies with the model. Chap. 3 focuses on our experiment conducted with ^{7}Li. First, in Sec. 3.1, the experimental setup is described. The sequence of the experiment is subject of Sec. 3.2. In these two sections it becomes clear that the experimental error bars are very small - a necessary condition for investigating laser cooling at resonance. In Sec. 3.3 the results of the experiment are presented and discussed. A large quantitative contradiction between the simple two-level theory of Chap. 2 and the experiment is shown. In particular, we uncover the possibility of laser cooling at resonance. The following chapter (Chap. 4) is dedicated to solving the contradiction. In Secs. 4.1 and 4.2 more complex and more realistic atomic models are analyzed, leading up to a full description of ^{7}Li in Sec. 4.3. The theory is compared to the experiment in Chap. 5. While good agreement is shown for certain parameter values, the small discrepancy which arises for on resonance parameters is explained by the dimensionality. Although the experiment is three-dimensional (3D) all of our theory is 1D. This leads to Chap. 6, where 3D Monte-Carlo simulations are presented. Choosing a simplified, semi-classical approach the somewhat surprising importance of coherent two-photon processes is shown. Finally, Chap. 7 concludes the thesis.

Chapter 2

Background: Laser Cooling a Two-Level Atom

In this first theoretical chapter the ground work is set. A two level atom with one ground state $|g\rangle$ and one excited state $|e\rangle$ is considered. The energetic difference between the two levels is $\hbar\omega_A$. By means of two counter-propagating laser beams of frequency ω_L it can be laser cooled down to the so-called Doppler limit. The theory presented here is four decades old [3–5] and very well known. For this reason only the main arguments and results will be given together with some of the technical details that will be relevant later. The interested reader is referred to a long list of good references [13–18]. Of course this list is in no way complete.

2.1 Intuitive Approach

Before starting any of the mathematics lets understand the underlying physical mechanism of laser cooling.

Imagine an atom moving with velocity v in 1D. A laser beam propagating in the same direction as the atom, i.e. $\vec{k}$ and $\vec{v}$ are parallel, will be Doppler shifted to the red (lower frequency) by an amount $-\vec{k}\cdot\vec{v} = -kv$. A laser beam propagat-

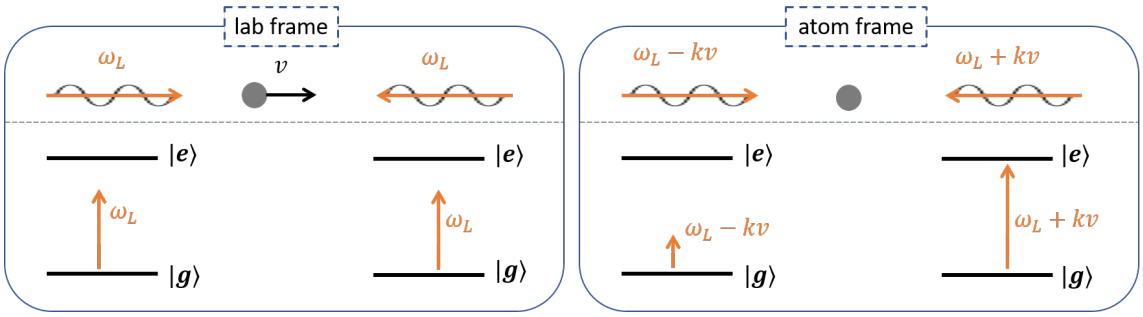

Figure 2.1: A two-level atom subject to red-detuned counter-propagating laser beams in the lab frame and in the atom rest frame.

ing in the opposite direction ($\vec{k}$ and $\vec{v}$ point in opposite directions) experiences a Doppler shift of $-\vec{k}\cdot\vec{v} = +kv$ into the blue. For laser cooling to work the atom is subjected to two laser beams: one from the left and one from the right. The frequency of the laser is chosen a little below the atomic frequency, so $\omega_L < \omega_A$. The Doppler shift then works in favor of the counter-propagating laser beam as illustrated in Fig. 2.1. The atom will preferably absorb counter-propagating photons and thus, due to momentum conservation, experience a decrease in momentum. The change of momentum per unit time can be written as a force. As the atom slows down the Doppler shift becomes smaller and the probability of absorbing from the counter-propagating beam decreases while the probability of absorbing from the co-propagating laser increases. Hence the force is weaker for low velocity. In fact, for small velocities the force is approximately proportional to the velocity. This, then, is a friction force: $F = -\alpha v$, where α is the friction coefficient. After a photon is absorbed it must be emitted. Since one typically works at low laser intensities spontaneous emission dominates. Therefore the emission direction is random and on average does not contribute to the change in velocity ($\langle v\rangle$ is not effected). It does, though, contribute to the second moment of v, so to $\langle v^2\rangle$. The simplest way to understand this is by realizing that spontaneous emission is nothing more than a random walk in momentum space. With this random walk a diffusion coefficient D is associated.

To sum up we have, on the one hand, a friction force which lowers the velocity (cooling) and on the other hand diffusion which increases the velocity (heating). One can thus think of the atom as if it were in an optical molasses. Since the atom is subject to both the force and the diffusion it will attain a steady state with which a steady state temperature is associated. This temperature is what we are interested in calculating.

2.2 The Density Matrix and its Evolution in Time

The system at hand includes a two-level atom and two laser beams. In addition there is an omnipresent radiation field, the quantized electromagnetic field, which we will assume to be in the vacuum state. A full quantum treatment consists of quantizing both the atomic and the radiation degrees of freedom. The information on these degrees of freedom is held in an infinite dimensional density matrix $\sigma(t)$. One then has to write the full Hamiltonian consisting of all system parts:

$$H_{\text{full}} = H_A + H_R + V_{AL} + V_{AR}\ . \tag{2.1}$$

The first two terms describe the atomic (H_A) and radiation (H_R) degrees of freedom while the latter two are interaction terms. The interaction of the atom with the laser light is given by V_{AL} and with the radiation field by V_{AR}. The evolution of the density matrix $\sigma(t)$ is given by the differential equation

$$\frac{d\sigma}{dt} = -\frac{i}{\hbar}\left[H_{\text{full}}, \sigma(t)\right]. \tag{2.2}$$

But this is a total overkill. The actual computation is not even possible given that $\sigma(t)$ is of infinite size. If we can get rid of the quantized electromagnetic field the calculation will be a much more feasible task.

The trick is to take the trace of $\sigma(t)$ over the radiation degrees of freedom and thus reducing it from infinite size to include just the atomic degrees of freedom. We define the atomic density matrix $\rho(t)$ via

$$\rho(t) = Tr_R[\sigma(t)] \tag{2.3}$$

and its components are

$$\rho(t) = \begin{pmatrix} \rho_{ee}(t) & \rho_{eg}(t) \\ \rho_{ge}(t) & \rho_{gg}(t) \end{pmatrix}, \tag{2.4}$$

where $\rho_{ij} = \langle i|\rho|j\rangle$ for $i, j = e, g$. The on-diagonal elements are the populations of the excited and ground state an thus must add up to unity, i.e. $Tr[\rho(t)] = 1$. The off-diagonal elements are the coherences. As a consequence of this trace not all terms in H_{full} are relevant. Only terms which explicitly depend on atomic degrees of freedom must be considered and so H_R becomes irrelevant. (Its commutator with $\rho(t)$ vanishes.)

Part of the quantum radiation field has been eliminated but it still remains in the interaction term V_{AR}. In order to get rid off this term the vacuum field is considered as a reservoir. This results in adding an extra term, γ_{dec}, to the equation of motion. It is given by

$$\gamma_{dec} = \Gamma \begin{pmatrix} -\rho_{ee}(t) & -\rho_{eg}(t)/2 \\ -\rho_{ge}(t)/2 & \rho_{ee}(t) \end{pmatrix}, \tag{2.5}$$

where $\Gamma = 1/\tau$ is the linewidth of the excited state and τ is the life time of an atom in the excited state. The physical significance of this term is spontaneous emission which arises due to the coupling of the atom to the vacuum field.

The equation of motion is then reduced to

$$\frac{d\rho}{dt} = -\frac{i}{\hbar}\left[H, \rho(t)\right] + \gamma_{dec} \tag{2.6}$$

and the Hamiltonian takes the simple form

$$H = H_A + V_{AL}. \tag{2.7}$$

The atomic Hamiltonian H_A contains the atomic degrees of freedom. By setting the energy of the ground state at $E = 0$ it is simply

$$H_A = \hbar\omega_A |e\rangle\langle e|. \tag{2.8}$$

Next we deal with the interaction term V_{AL}. Since the laser is in a coherent state its field can be described by a classical function of space and time $E_L(z,t)$. In addition we are dealing with weak fields so that the interaction is restricted to the dipole term. It is given by

$$V_{AL} = -d \cdot E_L(z,t), \tag{2.9}$$

where d is the induced dipole moment of the atom with magnitude d_0. Its operator is the sum of the raising and lowering operator, so

$$d = d_0 \left(|g\rangle\langle e| + |g\rangle\langle e|\right). \tag{2.10}$$

The electric field is

$$E_L = E_0 \cos(kz - \omega_L t) + E_0 \cos(kz + \omega_L t), \tag{2.11}$$

where the first (second) term describes the laser coming from the left (right) and propagating in the $+\hat{z}$ $(-\hat{z})$ direction and $k = \omega_L/c$ is the wave number. Using exponentials we get

$$E_L = E_0 \cos(kz)\, e^{-i\omega_L t} + c.c.\ . \tag{2.12}$$

Plugging Eqs. (2.10) and (2.12) into Eq. (2.9) we obtain

$$V_{AL} = \hbar\Omega(z) e^{-i\omega_L t} |e\rangle\langle g| + h.c.\ , \tag{2.13}$$

where the rotating wave approximation, which consists of neglecting off-resonance counter-rotating terms, was made. We have also defined the Rabi frequency $\Omega(z) = -d_0 E_0 \cos(kz)/\hbar$.

2.3 The Optical Bloch Equations

The Hamiltonian given by Eqs. (2.7), (2.8) and (2.13) is plugged into Eq. (2.6) together with the decay term (2.5). This results in four coupled differential equations for the density matrix components. One can get rid of the explicit time dependence

by moving into a frame, rotating at the laser frequency ω_L. The four equations are then

$$\begin{aligned} \frac{d\rho_{ee}}{dt} = -\frac{d\rho_{gg}}{dt} &= i\Omega\left(\rho_{eg} - \rho_{ge}\right) - \Gamma\rho_{ee} \\ \frac{d\rho_{ge}}{dt} = \left(\frac{d\rho_{eg}}{dt}\right)^{\star} &= i\delta\rho_{ge} + i\Omega\left(\rho_{gg} - \rho_{ee}\right) - \frac{\Gamma}{2}\rho_{ge}, \end{aligned} \tag{2.14}$$

where $\delta = \omega_L - \omega_A$ is the detuning of the laser light from resonance. Note that these equations can also be obtained directly from Eq. (2.6) by replacing $\omega_A \to \delta$ in Eq. (2.8) and $e^{-i\omega_L t}|e\rangle\langle g| \to |e\rangle\langle g|$ in Eq. (2.13). The effect of the rotating frame is therefore

$$\begin{aligned} \omega_A &\to \delta \\ e^{-i\omega_L t}|e\rangle\langle g| &\to |e\rangle\langle g|\,. \end{aligned} \tag{2.15}$$

By setting the lhs of Eqs. (2.14) equal to zero the steady state solution is obtained. Notice that the two equations for $d\rho_{ee}/dt$ and $d\rho_{gg}/dt$ are identical. One therefore adds an additional equation: $\rho_{gg} + \rho_{ee} = 1$, which is nothing more than the normalization condition.

At this point it is instructive to show a simple way for solving the equations numerically [19]. Although this is not necessary for the two-level system (the equations can be solved analytically) it will prove very helpful for the coming, more complicated models. First, rearrange the density matrix $\rho(t)$ in a vector $\vec{\rho}(t)$ as follows

$$\rho(t) = \begin{pmatrix} \rho_{ee}(t) & \rho_{eg}(t) \\ \rho_{ge}(t) & \rho_{gg}(t) \end{pmatrix} \quad \to \quad \vec{\rho}(t) = \begin{pmatrix} \rho_{ee}(t) \\ \rho_{eg}(t) \\ \rho_{ge}(t) \\ \rho_{gg}(t) \end{pmatrix}. \tag{2.16}$$

The OBE can then be be written compactly as

$$\frac{d}{dt}\vec{\rho}(t) = \overleftrightarrow{M} \cdot \vec{\rho}(t), \tag{2.17}$$

where the coefficient matrix $\overleftrightarrow{M}$ is given by

$$\overleftrightarrow{M} = \begin{pmatrix} -\Gamma & i\Omega & -i\Omega & 0 \\ i\Omega & -\Gamma/2 - i\delta & 0 & -i\Omega \\ -i\Omega & 0 & -\Gamma/2 + i\delta & i\Omega \\ \Gamma & -i\Omega & i\Omega & 0 \end{pmatrix}. \tag{2.18}$$

The steady state solution is found by taking the inverse of $\overleftrightarrow{M}$ and applying it to

a zero-vector. But because the first and last row are identical the inverse doesn't exist. To solve this problem, again, the normalization condition is used. The last line (or equivalently the first) is exchanged for the condition $\rho_{gg} + \rho_{ee} = 1$ and one obtains

$$\overleftrightarrow{M}_0 = \begin{pmatrix} -\Gamma & i\Omega & -i\Omega & 0 \\ i\Omega & -\Gamma/2 - i\delta & 0 & -i\Omega \\ -i\Omega & 0 & -\Gamma/2 + i\delta & i\Omega \\ 1 & 0 & 0 & 1 \end{pmatrix}. \tag{2.19}$$

To find the steady state solution the inverse of this matrix is applied to the vector $\vec{\rho}_0 = (0, 0, 0, 1)$, i.e.

$$\rho^{st} = \left(\overleftrightarrow{M}_0\right)^{-1} \cdot \vec{\rho}_0. \tag{2.20}$$

Given ρ^{st}, the force acting on and the diffusion coefficient felt by the atoms can be calculated after which, by finding their equilibrium, the temperature is obtained. In the following the results of such a procedure are stated. More detailed computations will be given in Chap. 4 where more realistic and more relevant atomic systems are considered. Here, for the simple two-level atom, intuitive arguments will be used. A full quantitative treatment can be found in the appropriate literature mentioned in the beginning of this chapter.

2.4 The Force

When a photon is absorbed by the atom its momentum is changed by an amount $\Delta p = \hbar k$ equal to the momentum carried by the photon. The characteristic time between two such events is $\Delta t = (\Gamma \rho_{ee})^{-1}$ and so the force is given by

$$F = \frac{\Delta p}{\Delta t} = \hbar k \Gamma \rho_{ee}. \tag{2.21}$$

It is clear that the direction of the force is given by the direction of the absorbed photon, i.e. the direction $\vec{k}$ in which the laser is propagating. The population of the excited state ρ_{ee} is given, in terms of the saturation parameter

$$s = \frac{2\,(\Omega/\Gamma)^2}{1 + 4\,(\delta/\Gamma)^2}, \tag{2.22}$$

by

$$\rho_{ee} = \frac{1}{2}\frac{s}{1+s}. \tag{2.23}$$

The functional dependence of F on δ is a Lorentzian - a well known result from quantum optics. If the atom is moving at velocity v the detuning seen by the atom

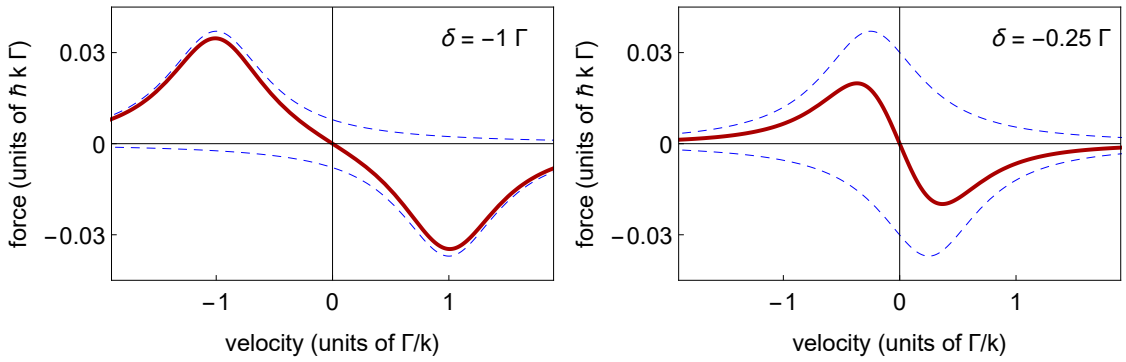

Figure 2.2: A plot of the force as a function of velocity for $\delta = -\Gamma$ (left) and $\delta = -0.25\ \Gamma$ (right). Here we have $\Omega = 0.2\ \Gamma$. The individual forces of the left and the right laser are shown blue dashed and their sum as a solid red line.

is Doppler-shifted by an amount $-\vec{k}\cdot\vec{v}$ such that we must replace

$$\delta \quad \rightarrow \quad \delta - \vec{k}\cdot\vec{v} \tag{2.24}$$

in Eq. (2.22). The force of the sum of two laser beams, one with $\vec{k} = +k\hat{z}$ and one with $\vec{k} = -k\hat{z}$, acting on an atom with velocity $\vec{v} = +v\hat{z}$ is given by

$$F(v) = \hbar k \frac{\Gamma}{2}\left[\frac{2\left(\Omega/\Gamma\right)^2}{1+2\left(\Omega/\Gamma\right)^2+4\left((\delta-kv)/\Gamma\right)^2} - \frac{2\left(\Omega/\Gamma\right)^2}{1+2\left(\Omega/\Gamma\right)^2+4\left((\delta+kv)/\Gamma\right)^2}\right]. \tag{2.25}$$

For $\delta < 0$, which is a necessary condition, the first (second) term is a Lorentzian in v centered around $-|\delta|$ ($|\delta|$). These two contributions are shown as dashed lines in Fig. 2.2. The total force $F(v)$ (solid line in Fig. 2.2) shows a linear dependence for $kv \ll \Gamma$ in agreement with the intuition given in Sec. 2.1. In this limit one can thus expand the force in a Taylor series to first order, such that $F \approx -\alpha v$ where α is the friction coefficient given by

$$\alpha = 8\hbar k^2 \frac{(-\delta)}{\Gamma} \frac{2\left(\Omega/\Gamma\right)^2}{\left[1+2\left(\Omega/\Gamma\right)^2+4\left(\delta/\Gamma\right)^2\right]^2}\ . \tag{2.26}$$

This is the nature of the cooling force. The atom experiences a friction force as if it were in a viscous fluid or molasses.

2.5 The Diffusion Coefficient

In general, the origin of diffusion is some kind of fluctuation. Here there are two fluctuating quantities. The first is spontaneous emission. The direction in which the photon is emitted is random while the step size ($\hbar k$) is much smaller than the total

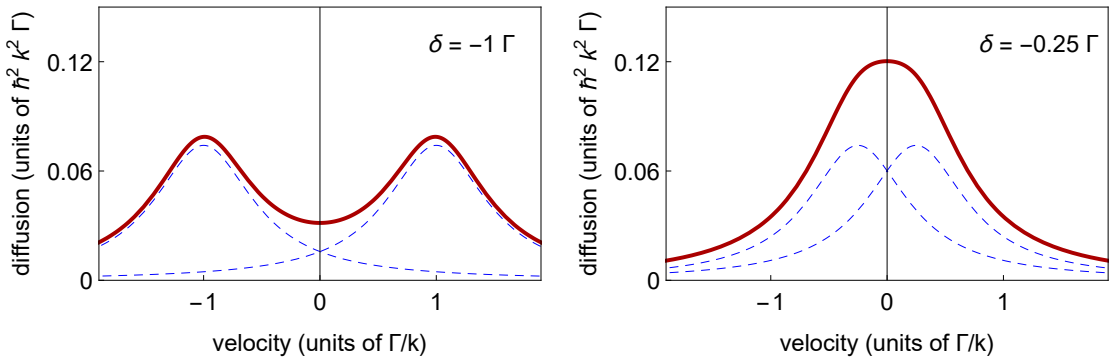

Figure 2.3: A plot of the diffusion coefficient as a function of velocity for $\delta = -\Gamma$ (left) and $\delta = -0.25\ \Gamma$ (right). Here we used $\Omega = 0.2\ \Gamma$ as in Fig. 2.2. The individual contributions are shown blue dashed and their sum as a solid red line.

momentum of the atom. The atom thus experiences a random walk in momentum space which can be quantified by a vacuum diffusion coefficient D^{vac}. We associate it with the electromagnetic vacuum field because spontaneous emission occurs due to the coupling of the atom with the vacuum field. The second fluctuating quantity has to do with the laser beams and is quantified by the laser diffusion coefficient D^{las}. Here it is the number of photons which are incident on the atom per unit time, and therefore the number of photons absorbed per unit time, that fluctuates. So while D^{vac} arises from fluctuations in the spontaneous emission, D^{las} has to do with fluctuations in the absorption. Because an absorption process is necessarily followed by an emission process we conclude that $D^{las} \approx D^{vac}$.

Lets find an expression for D^{vac}. By definition, a diffusion coefficient is half the change of the second moment of the momentum in time, i.e.

$$\frac{d}{dt}\langle p^2 \rangle = 2D^{vac}. \tag{2.27}$$

Since the step size is $\hbar k$ and the characteristic time is $\Delta t = (\Gamma \rho_{ee})^{-1}$ we get

$$D^{vac} = \frac{1}{2}\frac{(\Delta p)^2}{\Delta t} = \frac{1}{2}(\hbar k)^2 \Gamma \rho_{ee}\ . \tag{2.28}$$

The total diffusion coefficient, using $D^{las} \approx D^{vac}$, is then

$$D = D^{vac} + D^{las} = (\hbar k)^2 \Gamma \rho_{ee}\ , \tag{2.29}$$

where ρ_{ee} is given in Eq. (2.23). The contributions of the two lasers must now be added and we obtain an expression similar to Eq. (2.25) but with a plus instead of

a minus sign between the two terms:

$$D(v) = (\hbar k)^2 \frac{\Gamma}{2} \left[\frac{2\left(\Omega/\Gamma\right)^2}{1 + 2\left(\Omega/\Gamma\right)^2 + 4\left((\delta - kv)/\Gamma\right)^2} + \frac{2\left(\Omega/\Gamma\right)^2}{1 + 2\left(\Omega/\Gamma\right)^2 + 4\left((\delta + kv)/\Gamma\right)^2} \right] . \tag{2.30}$$

This function is plotted in Fig. 2.3. It experiences an extremum at $v = 0$ so the first order expansion is constant. For $kv \ll \Gamma$ we get

$$D(v) \approx D(0) = (\hbar k)^2 \Gamma \frac{2\left(\Omega/\Gamma\right)^2}{1 + 2\left(\Omega/\Gamma\right)^2 + 4\left(\delta/\Gamma\right)^2} . \tag{2.31}$$

2.6 The Temperature

2.6.1 Method 1: Fluctuation-Dissipation Theorem

A central result of statistical physics is the so-called Fluctuation-Dissipation theorem (FDT) [20, 21]. It states that any system experiencing dissipation will fluctuate and vice-versa. This happens because the physical mechanism causing dissipation also causes fluctuations. The fluctuating nature is thus intrinsic to dissipative systems. The laser cooled atom is a good example of this theorem. The absorption of photons leads to friction, i.e. dissipation, which is necessarily followed by spontaneous emission which, being a randon process, causes the atom to fluctuate in momentum space. If the dissipation is quantified by a friction coefficient α and the fluctuation by a diffusion coefficient D, the FDT says that, at a given temperature T, so in thermodynamic equilibrium, the two will be proportional to each other:

$$D = k_B T \alpha, \tag{2.32}$$

where k_B is the Boltzmann constant. Here, since we have found α and D in Eqs. (2.26) and (2.31), the theorem is applied to find the steady state temperature. One finds

$$k_B T = \frac{\hbar\Gamma}{2} \frac{\Gamma}{4(-\delta)} \left[1 + 2\left(\frac{\Omega}{\Gamma}\right)^2 + 4\left(\frac{\delta}{\Gamma}\right)^2 \right] . \tag{2.33}$$

The temperature dependence on the detuning is plotted in Fig. 2.4. For vanishing intensity ($\Omega \ll \Gamma$) and $\delta = -\Gamma/2$ the temperature reaches its minimum value

$$k_B T_D = \frac{\hbar\Gamma}{2} \tag{2.34}$$

called the Doppler limit. As the laser light approaches resonance, i.e. $\delta \to 0$, the temperature diverges.

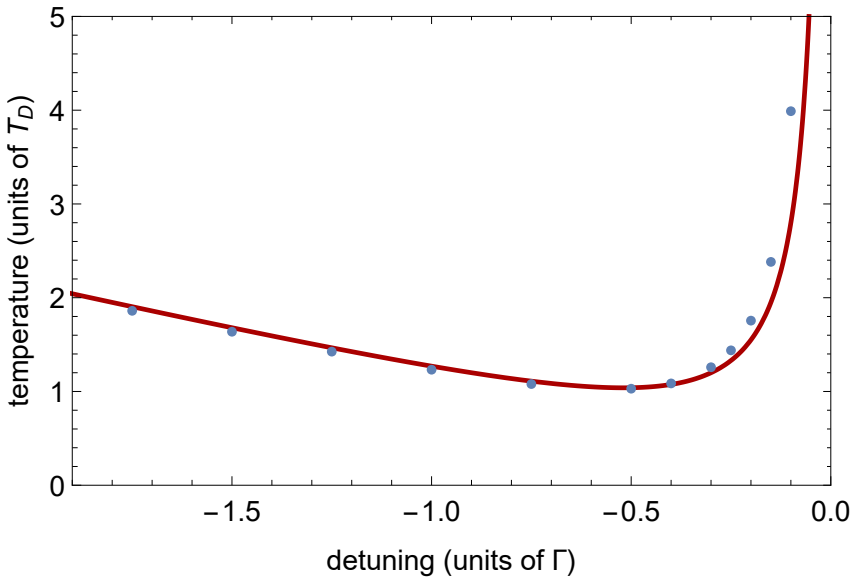

Figure 2.4: A plot of the temperature as a function of detuning for $\Omega = 0.2\,\Gamma$. The solid line is the analytical expression given in Eq. (2.33). The dots are obtained by using the exact velocity distribution and fitting to a Gaussian.

2.6.2 Method 2: Fokker-Planck Equation

In this section an alternative method for finding the temperature is discussed. While using the FDT is the normal approach, the procedure introduced here is equivalent in the limit $kv \ll \Gamma$ but can give predictions also outside this limit. This will become important in the following chapters, where for $kv \ll \Gamma$ the nature of the force changes abruptly. The essence of this procedure is to take the full velocity distribution into account, contrary to the FDT approach which only considers its moments.

We mentioned above that the atom in the laser light is like a particle doing a random walk inside a viscous fluid or an optical molasses. The macroscopic description of such a process is given by the Fokker-Planck equation (FP)

$$\frac{\partial W(v,t)}{\partial t} = -\frac{\partial}{\partial(mv)}F(v)W(v,t) + \frac{\partial^2}{\partial(mv)^2}D(v)W(v,t), \tag{2.35}$$

where $W(v,t)$ is the velocity distribution at time t. The steady state solution is given by

$$W(v) = \frac{A}{D(v)}\exp\left[\int \frac{F(v')}{D(v')}d(mv')\right], \tag{2.36}$$

where the integration constant A can be used for normalization. If we plug in the linearized force $F = -\alpha v$, where α is given in Eq. (2.26), and the constant diffusion

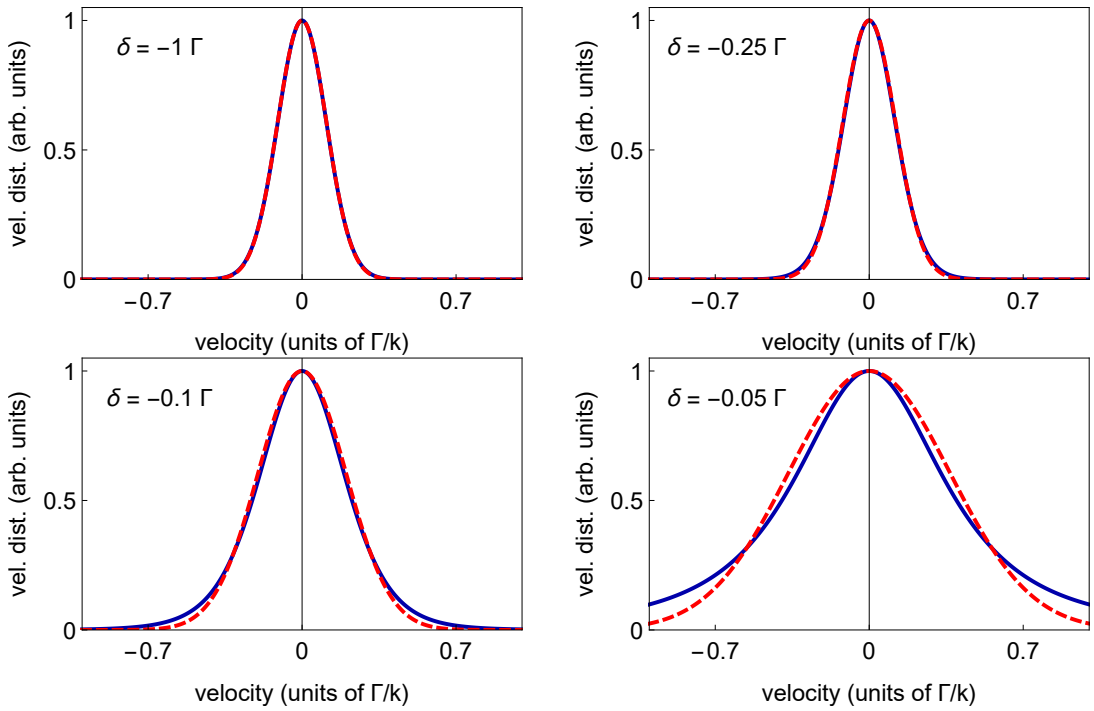

Figure 2.5: A plot of the exact velocity distribution (blue solid) for $\delta = -\Gamma$ (top left) and $\delta = -0.25\ \Gamma$ (top right). Here we used $\Omega = 0.2\ \Gamma$ and $\omega_r = 0.01\ \Gamma$. The Gaussian fit is shown red dashed. As $\delta \to 0$ (bottom figures) the distribution deviates from a Gaussian.

coefficient D from Eq. (2.31) a Gaussian distribution, given by

$$W(v) = C \exp\left[-\frac{m\alpha}{2D}v^2\right] \tag{2.37}$$

is obtained, in agreement with Maxwell-Boltzmann statistics. The width of this distribution is $\langle v^2 \rangle = D/m\alpha$ which is related to the temperature via the equipartition theorem in 1D

$$k_B T = m\langle v^2 \rangle = \frac{D}{\alpha}. \tag{2.38}$$

The FDT is thus rederived in the limit $kv \ll \Gamma$.

But we do not have to limit ourselves to a small velocity range. The exact expressions for the force and the diffusion coefficient, given in Eqs. (2.25) and (2.30), can be directly plugged into Eq. (2.36), which leads to the exact velocity distribution $W(v)$. This integral has an analytic solution given by

$$W(v) = \frac{A}{D(v)}\left[1 + 2\left(\frac{\Omega}{\Gamma}\right)^2 + 4\left(\frac{\delta}{\Gamma}\right)^2 + 4\left(\frac{kv}{\Gamma}\right)^2\right]^{-|\delta|/2\omega_r}, \tag{2.39}$$

where $\omega_r = \hbar k^2/2m$ is the recoil frequency of the atom. In Fig. 2.5 this function is plotted for different values of δ together with a Gaussian fit. We see that only when the detuning δ becomes vanishingly small the difference between $W(v)$ in Eq. (2.39)

and a Gaussian can be seen. This justifies the linear and constant approximations for the force and the diffusion coefficient respectively, provided we use "normal" values for δ.

The temperature can be extracted from the distribution in Eq. (2.39) by fitting to a Gaussian, using the width $\langle v^2 \rangle$ as a fitting parameter. Via the equi-partition theorem $\langle v^2 \rangle$ is converted to the temperature. The results of such a procedure are shown in Fig. 2.4 and produce an almost perfect match for "normal" detuning values. As $\delta \to 0$ the FP procedure deviates from the FDT approach. Considering the non-Gaussian velocity distribution found in this regime, this was to be expected.

2.7 Previous Experimental Results

Experimental verification of Eq. (2.33), and in particular of the Doppler limit [Eq. (2.34)], is not simple. This has two main reasons. First of all, no real atom has just two levels. Because of conservation of angular momentum only transitions $J_g \to J_e = J_g + 1$, where J_g and J_e are the angular momentum of the ground and excited state respectively, can be used for laser cooling. Therefore, even for $J_g = 0 \to J_e = 1$, the excited state possesses a Zeeman degeneracy and for $J_g > 0$ both the ground state and the excited state are degenerate. For open-shell lanthanides, which have a large electronic spin, it has been shown [22] that at large detuning ($\delta \lesssim -15\ \Gamma$) and intensity ($I \approx 50\ I_{sat}$ per beam) the atomic cloud becomes almost completely spin polarized. The Zeeman degeneracy is then lifted inside the magnetic field gradient (~ 1.71 G/cm) of the magneto-optical trap. Such a scheme is impractical for us though, since the Doppler limit is reached for vanishing intensity and small detunings. Moreover, ^{7}Li, which is what we use in our experiment, does not posses a large electronic spin. The second reason is sub-Doppler cooling. An atomic transition with a degenerate ground state is cooled far below the Doppler limit without changing the experimental setup. Historically, this first came as a surprise [7] but was then explained shortly after [23] as the effect of a polarization gradient on a degenerate ground state. While this phenomenon will be discussed in detail in Sec. 4.2, note here that in order to verify Eq. (2.33) one must use an atomic species in which sub-Doppler cooling does not work. Three examples, namely Helium, Mercury and Lithium, are reviewed here.

2.7.1 Helium

Using meta-stable ^{4}He, it was possible to experimentally observe the Doppler limit at "normal" laser parameters [24]. The results are shown in the left plot of Fig. 2.6 and agreement with the two-level theory is shown. The experiment was conducted in the

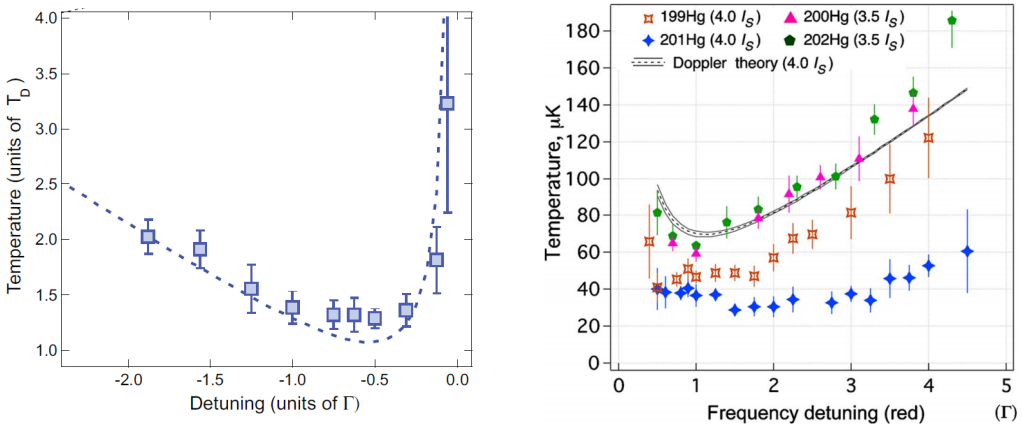

Figure 2.6: *Left*: The temperature of ^{4}He atoms in a three-dimensional optical molasses as a function of the detuning. The total intensity (sum of all six beams) is $I = 0.1\ I_{sat}$, where $I_{sat} = 165\ \mu\text{W/cm}^2$. The squares with one standard deviation error bars are the measurement and the dashed line is the two-level atom prediction [Eq. (2.33)]. Extracted from Chang et.al. (2014) [24]. *Right*: The temperature of bosonic and fermionic mercury isotopes in a three-dimensional optical molasses as a function of the detuning. The total intensity (sum of all six beams) is $I = 3.5\ I_{sat}$ ($I = 4\ I_{sat}$) for the bosons (fermions), where $I_{sat} = 1.02\ \text{W/cm}^2$. Extracted from McFerran et.al. (2010) [25].

limit $\Omega \ll \Gamma$, which is related to the laser intensity via $I/I_{sat} = 2(\Omega/\Gamma)^2$, where I_{sat} is the saturation intensity of the atomic transition. The minimal temperature observed corresponds to the Doppler limit. In addition, the sub-Doppler capture velocity is below one recoil velocity ($\hbar k/m$) and thus cannot work. A similar reasoning will be used by us when discussing ^{7}Li (Sec. 4.3).

2.7.2 Mercury

Of the four most abundant mercury isotopes, two are bosons (^{200}Hg and ^{202}Hg) and two are fermions (^{199}Hg and ^{201}Hg). The experimentally determined [25] detuning dependence of the temperature for all four isotopes is shown in the right plot of Fig. 2.6.

The cooling transition of the bosons is $J_g = 0 \rightarrow J_e = 1$ which results in temperatures very similar to that of a two-level atom (see Sec. 4.1 and especially Fig. 4.6). The experiment shown in Fig. 2.6 was done at a total laser intensity of $I = 3.5\ I_{sat}$. The general behavior of the two-level theory [Eq. (2.33)] is shown but the temperatures are far above the Doppler limit ($T_D = 31\ \mu\text{K}$) due to the high intensity.

For the fermions the cooling transition depends on the isotope. In the case of ^{199}Hg it is $J_g = 1/2 \rightarrow J_e = 3/2$ for which a $\sigma^+ - \sigma^-$ laser configuration (see

Sec. 4.1.2) does not permit sub-Doppler cooling. The experiment therefore recovers results that qualitatively agree with the two-level theory although they are ~ 20 μK below the prediction. The ^{201}Hg isotope is cooled on a $J_g = 3/2 \rightarrow J_e = 5/2$ transition. The ground state degeneracy of this isotope is large enough to give rise to sub-Doppler cooling.

2.7.3 Lithium

Our experiment, which is described in the next chapter, is conducted with bosonic lithium (^{7}Li). A few years ago [26], when my predecessors were producing a lithium BEC, they found a minimal temperature of $T \approx 300$ μK in the Doppler cooling stage. Since $T_D = 142$ μK for ^{7}Li this corresponds to ~ 2 T_D. In a different setup [27], very similar to ours and using laser parameters equivalent to ours, a minimum temperature of $T = 300 \pm 50$ μK was found. This consistent factor of ~ 2, which at the time was not given much attention, is understood by us and will be explained in Sec. 4.3.

Chapter 3

Experiment

3.1 Preparation of the Experiment

The goal of the experiment is to measure the steady state temperature of a gas of lithium atoms (^{7}Li) cooled on the D_2-line as a function of the detuning with high precision. The experimental errors of both the temperature and the detuning must be kept as low as possible. For this a series of preparatory steps are made. Starting from an already existing system [28], which utilizes diode lasers in a master-slave scheme, a few alternations were made serving the high precision goal.

3.1.1 Short Review of the System and the Atomic Transition

A DL 100 pro design (Toptica photonics) external cavity diode laser serves as the master laser. It is locked to the atomic transition (D_2-line of ^{7}Li) using saturated absorption spectroscopy and feeds four slave lasers. Two of them are used for the Zeeman slower and the other two for the magneto-optical trap (MOT). Each of these need two, spatially overlapping, lasing frequencies due to the multi-level structure of ^{7}Li which is shown in Fig. 3.1. The first laser, called the pump (red arrow in Fig. 3.1), can excite atoms out of the $|F = 2\rangle$ ground state while the repump (blue arrow) is responsible for the transitions starting at $|F = 1\rangle$. The MOT laser is split into six beams which are directed at the atoms from six orthogonal and anti-parallel directions. Before entering the glass chamber each pair of counter-propagating laser beams is given a $\sigma^+ - \sigma^-$ polarization. This is essential for the spatial trap, the MOT, to work. Precisely these beams will be used for the laser cooling experiment (optical molasses) described below.

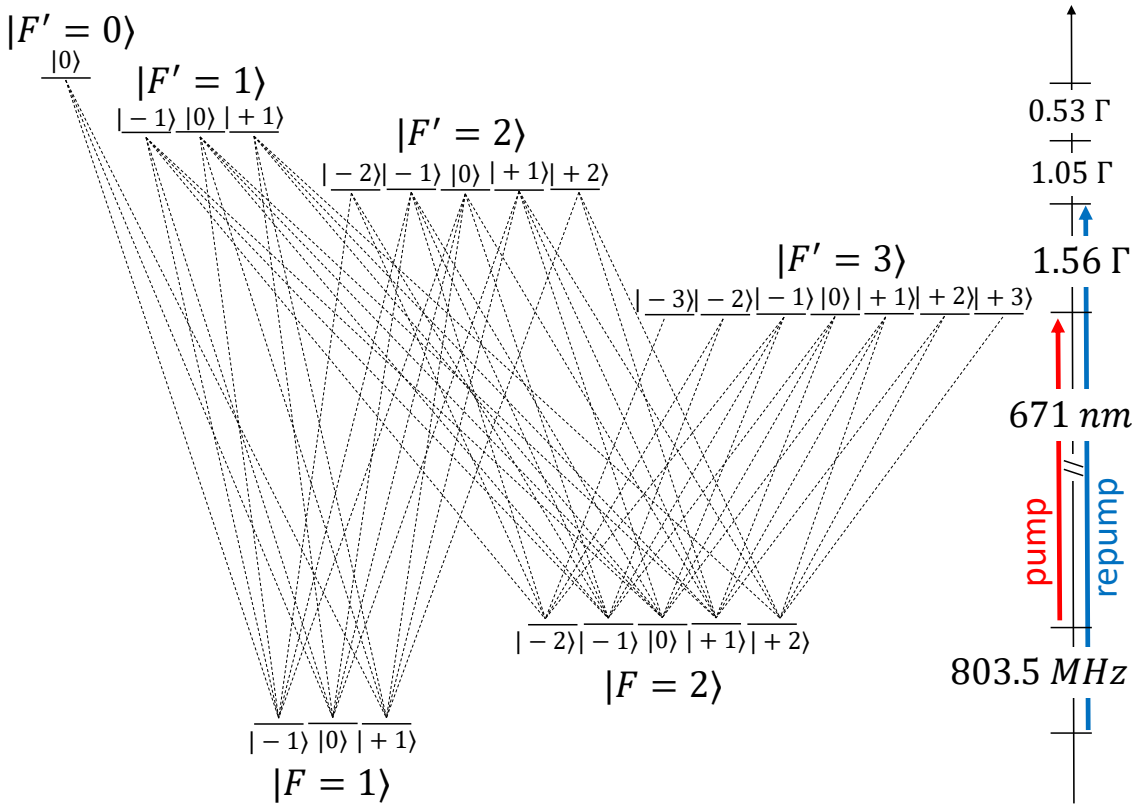

Figure 3.1: The hyper-fine structure of the D_2-line of ^{7}Li. The two ground states ($|F = 1, 2\rangle$) and four excited states ($|F' = 0, 1, 2, 3\rangle$) are shown together with their degenerate Zeeman sub-levels and the allowed dipole transitions (dotted lines). The Clebsch-Gordan coefficients are listed in Tables 4.3 and 4.2. On the right the energy spacing is shown. The main transition of the pump (repump) laser is depicted as a red (blue) arrow.

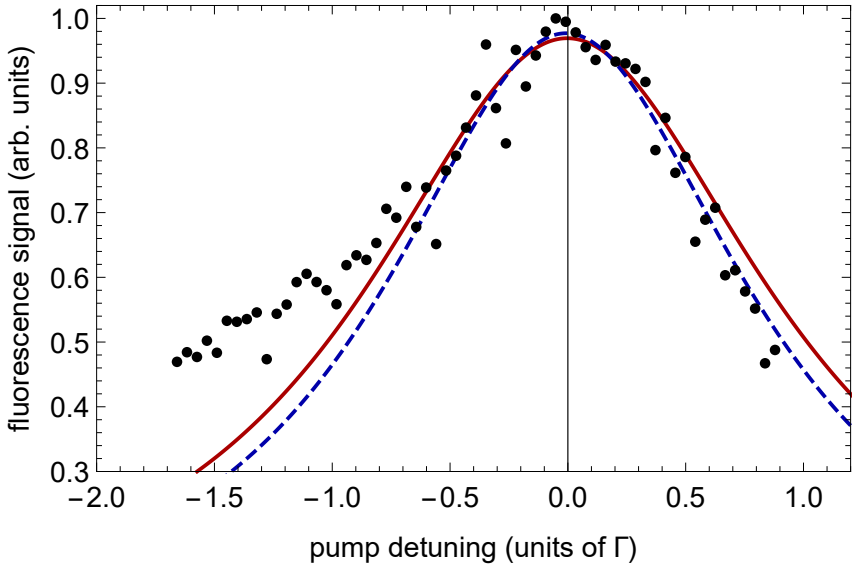

Figure 3.2: Fluorescence signal used to experimentally locate the position of the resonance. Since the data is not symmetric it cannot be fitted to a Lorentzian on the entire range (see text for explanation). We use only the central points and find a very low dependence of the position of the resonance on the range chosen. The red solid line is the fit to 21 central points while the blue dashed line uses 31 points. The shift in position of the fit maximum defines the uncertainty in resonance position.

3.1.2 Locking of the MOT Lasers

The locking mechanism of the already existing system used a feedback loop that was wired to the piezoelectric element on which the grating of the laser cavity is mounted. This scheme is standard and works well but its locking bandwidth is limited to ~ 2 kHz by the mechanical response of the piezo. A typical laser width of ~ 300 kHz was obtained.

In order to improve the locking bandwidth and laser width we wire the feedback loop to the current that runs the diode laser. This eliminates the slow mechanical response of the piezo. A locking bandwidth of ~ 50 kHz (improved by factor of ~ 25) and a laser width below 100 kHz were obtained. This provides us with an accuracy of laser frequency determination of $\leq 0.02\ \Gamma$, where $\Gamma/2\pi = 5.9$ MHz is the natural linewidth of the D_2-line of lithium atoms.

3.1.3 Locating the Resonance

After having obtained an improved laser frequency stability we turn to precise determination of the absolute frequency. For this we must find the transition $|F = 2\rangle \rightarrow |F' = 3\rangle$, which is the main transition of the pump laser, and set its frequency at $\delta = 0$. To do so, the atoms are loaded into the MOT and, after a short time of flight (TOF), their fluorescence signal measured. To take the picture

a short (100 μs) and strong ($I/6 = 0.7\ I_{sat}$ per beam, where $I_{sat} = 2.54$ mW/cm^2 is the saturation intensity) pulse of the MOT beams is used and the scattered light collected by a pco.pixelfly camera. The main feature of the pulse is that we use only the pump laser in order to isolate the main (closed) transition. The fluorescence signal as a function of the pump detuning is shown in Fig. 3.2 and fitted to a Lorentzian curve. The position of its maximum is defined as $\delta = 0$.

A few points should be noted:

1. If both the pump and repump lasers were used the fluorescence signal would show three distinct peaks, one for each transition $|F = 2\rangle \rightarrow |F' = 3, 2, 1\rangle$. An atom which is excited into $|F' = 2, 1\rangle$ can decay into $|F = 1\rangle$ (open transition) from where the repump brings it back again. But if the repump is switched off this does not happen and the signal is suppressed.

2. The fluorescence signal of a perfectly isolated transition is described by a symmetric Lorentzian line shape. As can be seen in Fig. 3.2 our data is not symmetric though. The reason is the optical pumping mentioned in point 1. For $\delta > 0$ the frequency approaches resonance with the transition $|F = 2\rangle \rightarrow |F' = 2\rangle$ which pumps the atoms into a dark state. This does not happen for $\delta < 0$ and so an atom scatters, on average, more photons for $\delta < 0$. The fluorescence signal therefore depends on the sign of δ.

In order to deal with the asymmetry of the signal only the central points are used for the fit. As a fitting function we use a symmetric Lorentzian curve with no overall offset and the range of the points used is varied. The fit obtained for the smallest (largest) range is shown in Fig. 3.2 as a red solid (blue dashed) line. As a function of number of points used, the position of the maximum changes only by a little (standard deviation of 0.02 Γ). Also the error in the fit (one standard deviation) is almost always below and typically far below 0.03 Γ. We thus estimate, taking into account both the laser width and the absolute frequency, a maximal error of $\sim 0.05\ \Gamma$ in the determination of the frequency.

3.1.4 Eliminating Potential Systematic Errors

Before going on and describing the experiment and its results we must be sure that no systematic errors exist. For this we calculate the residual AC stark shift during the short and intense pulse used for the frequency determination and the less intense optical molasses in which the atoms are cooled (see next section). Two effects must be taken into consideration:

1. The nearby ($\Delta = 1.56\ \Gamma$, see Fig. 3.1) transition $|F = 2\rangle \rightarrow |F' = 2\rangle$ causes a

shift in the energy level of the $|F = 2\rangle$ ground state. The atomic frequency of the main transition is thus altered.

2. The atoms in the cloud have a finite velocity. If the largest velocity present is v_{max}, the detuning is enhanced by an amount kv_{max} due to the Doppler shift. For our estimation of the systematic error we choose v_{max} corresponding to a temperature of $T = 2\ T_D$.

In order to calculate the AC stark shift of the $|F = 2\rangle$ state, we use the pump interaction potential $V_{AL}^{(p)}$ [see Eq. (4.49)] and take a partial trace over the relevant transitions. We find an upper bound of $-0.1\ \Gamma$ for the shift during the short and intense pulse and $-0.05\ \Gamma$ during the optical molasses. The two shifts result in a maximal systematic error of $0.05\ \Gamma$ and is therefore already contained in the experimental error.

3.2 Experimental Sequence

The experiment comprises of the following steps:

1. The MOT is loaded with $\sim 2 \times 10^7$ atoms. This number is relatively low and ensures a minimum of undesired atom-atom interactions.

2. The atoms are cooled to $T \sim 2\ T_D$ inside the MOT. This is the initial condition for the experiment.

3. Turning off the magnetic fields (no more spatial confinement) puts the atoms in the optical molasses. The detuning of the repump is brought to resonance with the $|F = 1\rangle \rightarrow |F' = 2\rangle$ transition and the pump detuning is set to the target value δ. The intesities of the pump and the repump are set to $I_p/6 = 0.06\ I_{sat}$ and $I_r/6 = 0.15\ I_{sat}$ respectively. All of the above is done simultaneously.

4. The atoms are subject to the optical molasses at pump detuning δ for a time period t_{mol}.

5. After the time t_{mol} has elapsed the laser beams are turned off and a time-of-flight (TOF) measurement of the temperature is conducted.

A typical TOF measurement is shown in Table 3.1. As the time increases the atomic cloud grows and the initial anisotropy, which is due to a small intensity imbalance of the six MOT beams, is lost. The width σ of the distribution is found by integrating the image in one direction and fitting it to a Gaussian density distribution

$$n(x) = n_0 \exp\left[-\frac{x^2}{2\sigma^2}\right] , \tag{3.1}$$

	TOF (ms)	σ (mm)		TOF (ms)	σ (mm)
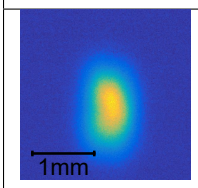	0.6	1.10	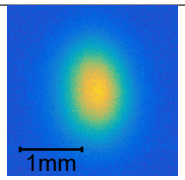	1.8	1.6
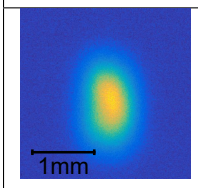	0.9	1.21	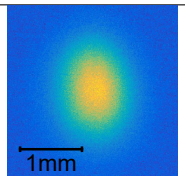	2.1	1.79
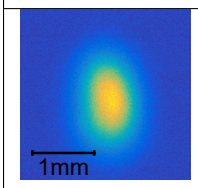	1.2	1.34	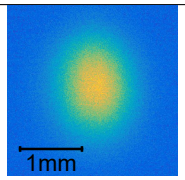	2.4	1.93
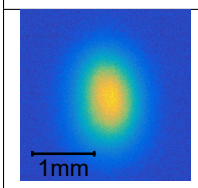	1.5	1.49			

Table 3.1: Fluorescence image of the atomic cloud for different times-of-flight (TOF) and the size σ of the Gaussian distribution.

where n_0 is a normalization constant. During the TOF each atom's motion is ballistic and hence the width of the atomic cloud evolves according to $\sigma(t) = \sqrt{\sigma_0^2 + \langle v^2 \rangle t^2}$, where σ_0 is the initial size and $\langle v^2 \rangle$ is the velocity distribution. At large times the width approaches $\sigma(t) \sim \sqrt{\langle v^2 \rangle} t$ and thus, since $\langle v^2 \rangle$ is isotropic, the atomic cloud becomes isotropic. In addition the finite waist size $w = 5.38$ mm of the MOT beams must be taken into account. Since the pulse intensity used for the fluorescence image is strongest at the center and weaker towards the edge we fit out data of $\sigma(t)$ from Table 3.1 to the function

$$\sigma(t) = \sqrt{(\sigma_0^2 + \langle v^2 \rangle t^2) \, \frac{w^2}{w^2 + \langle v^2 \rangle t^2}} \tag{3.2}$$

as shown in Fig. 3.3. For the data shown here, which was obtained for $\delta = 0$ and $t_{mol} = 1$ ms, the fit returns $\sigma_0 = 1.02$ mm and $\sqrt{\langle v^2 \rangle} = 74$ cm/s. Using the first equality of Eq. (2.38) and plugging in the mass of ^{7}Li this velocity distribution is equivalent to a temperature of $T = 460$ μK$= 3.25\, T_D$.

For each value of δ, the experimental steps and the fitting procedure outlined above is repeated for different values of t_{mol}. The temperature is then plotted as a function of the molasses time as shown in Fig. 3.4. This data is fitted to

$$T(t_{mol}) = T_{st} - (T_{st} - T_0)\, e^{-t_{mol}/\tau} \, , \tag{3.3}$$

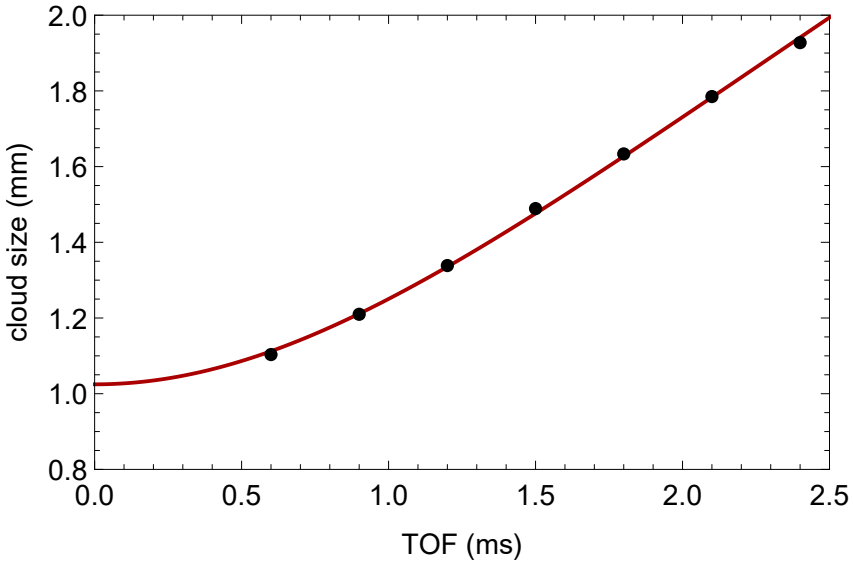

Figure 3.3: The measured size of the density distribution (see Table 3.1) is plotted as a function of the TOF. For this set of data we used $\delta = 0$ and $t_{mol} = 1$ ms. The error, which is one standard deviation of the Gaussian fit, is smaller then the point size. The data is fit to Eq. 3.2 and a velocity distribution of $\sqrt{\langle v^2 \rangle} = 0.74$ m/s is extracted together with the initial size $\sigma_0 = 1.02$ mm.

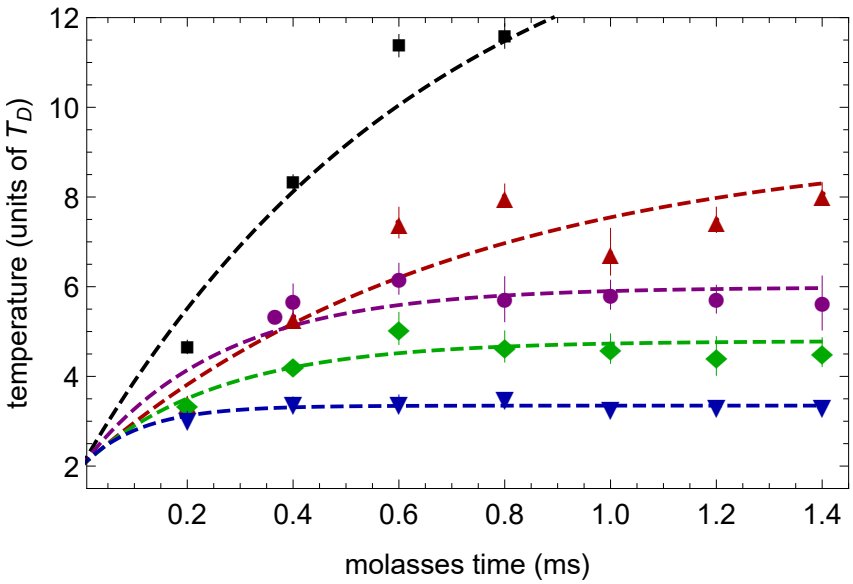

Figure 3.4: Experimental points and fit for the temperature as a function of the duration of the molasses, after the atoms are cooled to $T_0 \approx 2\ T_D$ in the MOT, for different values of the pump detuning. Blue upside down triangles: $\delta/\Gamma = 0$, green diamonds: $\delta/\Gamma = 0.2$, puple circles: $\delta/\Gamma = 0.25$, red triangles: $\delta/\Gamma = 0.3$, black squares: $\delta/\Gamma = 0.34$. The steady state temperature is extracted as a fitting parameter. For $\delta = 0.34\ \Gamma$ the temperature does not reach a steady state but all others do. Note that all detunings are positive.

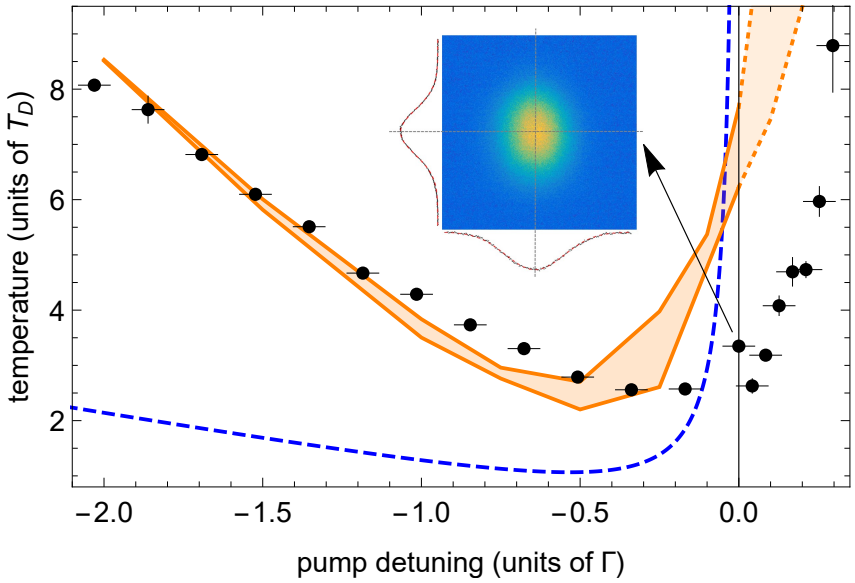

Figure 3.5: Plot of the measured temperature as a function of detuning. The error in the detuning is 0.05 Γ (see text). The error depicted for the temperature is one standard deviation of the fitting (dashed lines in Fig. 3.4). A typical atomic cloud at $\delta = 0$ after a long TOF (2.4 ms) is shown in the inset. The standard two-level theory is shown as a blue dashed line. The estimated interval obtained by numerically solving the 24 level + polarization model (see Sec. 4.3) is shown as an orange region. The parameters for the calculation are derived from the experiment and given by $\Omega_p = 0.26\ \Gamma$, $\Omega_r = 0.4\ \Gamma$ and $\delta_r = 0$.

where the steady state temperature T_{st} and the time constant τ are fitting parameters and $T_0 = 2\ T_D$ is given by the initial condition of the experiment (see point 2 of the sequence).

This long procedure makes clear that the steady state temperature T_{st} is obtained as a fitting parameter from a large amount of experimental data, rendering it very trustworthy.

3.3 Experimental Results

3.3.1 Temperature VS Detuning

The fitting parameter T_{st} from Fig. 3.4 is plotted as a function of the pump detuning in Fig. 3.5 and compared to the analytical solution of the simple two-level atom [see Eq. (2.33)]. It is clear that this simple theory does not describe the experiment at all:

- The Doppler limit is not reachable experimentally. The minimal temperature is a factor of ~ 2 larger. This deviation from the two-level theory is already known from other experiments with ^{7}Li [26, 27].

- For large negative detunings the measured temperature is much larger. Part of this effect can be explained by considering the additional heating present for an atom with a degenerate ground state as is discussed in Sec. 4.2.2.

- The most striking discrepancy is found for $\delta = 0$. The experiment clearly shows a (relatively low, $T \approx 3.35\ T_D$) steady state temperature while the two-level theory predicts $T \to \infty$. The fact that the temperature measured is indeed a steady state temperature can clearly be seen in Fig. 3.4, where the time evolution of the temperature at $\delta = 0$ is shown as blue upside down triangles. This observation is the central experimental result of this thesis. The explanation of the phenomenon is the subject of Sec. 4.3 in which the orange region of Fig. 3.5 is computed.

- Not only at $\delta = 0$, but for all $\delta \lesssim 0.3\ \Gamma$ a steady state temperature is observed. Only as the detuning approaches $\delta \approx 0.34\ \Gamma$ the cooling mechanism fails and the temperature diverges. In the experiments with $\delta > 0$ a slight loss ($\sim 20\%$) in the number of atoms is observed as a function of t_{mol}. This can be attributed to an imbalance in the MOT beams. Naturally, the atoms become more vulnerable to such an imbalance as the laser light is close to resonance or blue detuned.

- A typical fluorescence image of the atomic cloud at resonance ($\delta = 0$) is shown in the inset of Fig. 3.5. When integrating in either direction a perfect Gaussian is found. Therefore Maxwell-Boltzmann statistics apply and the temperature is well-defined. This is true for almost the entire detuning range investigated. Only in the large blue detuned regime ($\delta \gtrsim 0.3\ \Gamma$) deviations from a Gaussian are observed.

The temperature was also measured as a function of the repump detuning while holding the pump detuning constant at $\delta = 0$. It was found that the temperature is highly insensitive to this parameter over a large range.

3.3.2 Temperature VS Intensity

In a simplified version of the experimental sequence presented above, the temperature is measured as a function of the pump and repump intensity. Instead of going through the entire procedure of finding the temperature as a function of the molasses time and fitting to Eq. (3.3), we use $t_{mol} = 1.4$ ms and measure the temperature by means of TOF. Both detunings are set to resonance and the repump (pump) intensity per beam is $I_r/6 = 0.15\ I_{sat}$ ($I_p/6 = 0.06\ I_{sat}$) while the pump (repump) intensity I_p (I_r) is varied. The experimental data, which is shown in Fig. 3.6, is

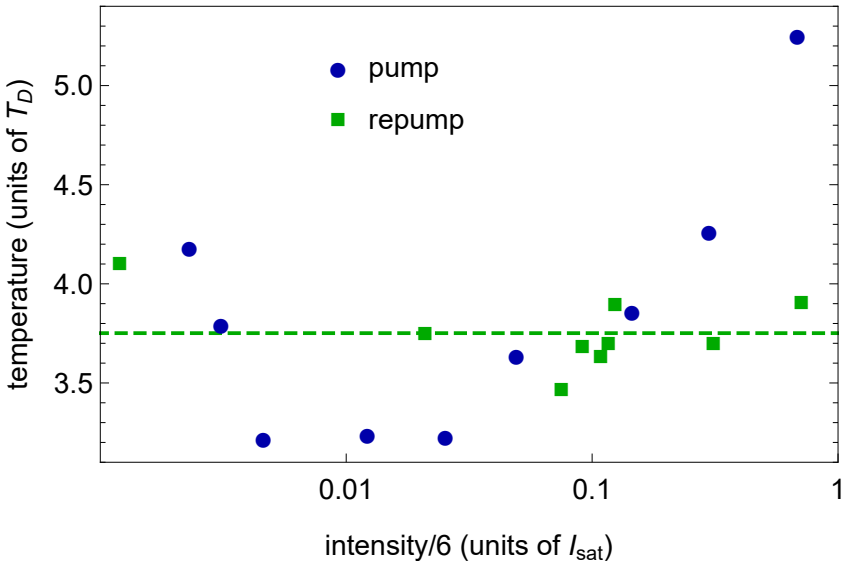

Figure 3.6: Measurement of the steady state temperature at $\delta = 0$ as a function of the pump or repump intensity. As can be seen there is an optimum in the pump intensity while the experiment is insensitive to the repump intensity. The green dashed line is the average temperature for the repump measurements (green squares).

found to be highly insensitive to the repump intensity. For the pump laser though, the behavior qualitatively agrees with the simple Doppler cooling model: the temperature decreases with decreasing intensity. For too low intensities, laser cooling fails and the temperature rises again.

Chapter 4

Theoretical Analysis

4.1 The $J_g = 0 \rightarrow J_e = 1$ Transition

Taking up what was started in Chap. 2 we now go a step further by considering an atom with a three-fold degenerate excited state, namely the transition $J_g = 0 \rightarrow J_e = 1$. As in Chap. 2, the atomic frequency is given by ω_A and the laser frequency by ω_L. The laser is tuned slightly below the atomic transition such that $\delta = \omega_L - \omega_A < 0$. The degenerate structure of the excited state allows the introduction of selection rules. Here a special laser polarization configuration, which is also used in the experiment, is considered, namely $\sigma^+ - \sigma^-$. This section serves as an intermediate step before reaching the full picture of a multi-level atom and in particular ^{7}Li in Sec. 4.3. Both the mathematics and the technical details will be stressed. While the $J_g = 0 \rightarrow J_e = 1$ system is relatively simple the ^{7}Li system is quite complex. The goal is to understand the procedure here and apply it later.

4.1.1 The Atomic System

The atom at hand has one ground state ($|g\rangle$) and three degenerate excited states ($|e_{\pm 1}\rangle$ and $|e_0\rangle$), where the subscript denotes the magnetic quantum number. A schematic is shown in Fig. 4.1 together with the allowed dipole transitions which arise due to conservation of angular momentum. If the laser light carries a pure left-handed (right-handed) polarization σ^- (σ^+), i.e. the photon angular momentum is -1 ($+1$), the only possible transition is $|g\rangle \rightarrow |e_{-1}\rangle$ ($|g\rangle \rightarrow |e_{+1}\rangle$). For linear polarization Π (so 0 photon angular momentum) only $|g\rangle \rightarrow |e_0\rangle$ is allowed. The coupling constant of a transition is proportional to its Clebsch-Gordan coefficient.

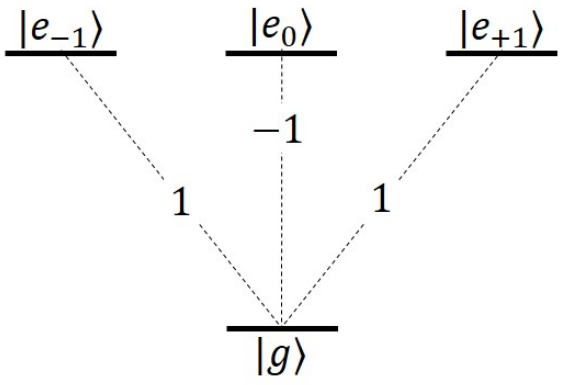

Figure 4.1: The four atomic levels of the $J_g = 0 \rightarrow J_e = 1$ transition. The Clebsch-Gordan coefficents of the allowed dipole transitions are shown.

4.1.2 The $\sigma^+ - \sigma^-$ Laser Configuration

When discussing the experiment we noted that the same laser beams that are used for the MOT are also used for the optical molasses. The polarization configuration is thus given. Each two counter propagating laser beams must have an opposite circular polarization. Otherwise the MOT would not work. Our mathematical model is 1D in which case this configuration is called $\sigma^+ - \sigma^-$.

The laser field at position z and time t is given by the sum of two lasers. The laser coming from the left (right) and propagating along $+\hat{z}$ $(-\hat{z})$ carries left-handed (right-handed) circular polarization σ^- (σ^+). The two are given by

$$E_{\text{left}}(z,t) = \sqrt{2}E_0\left[-\cos(kz - \omega_L t)\,\hat{x} + \sin(kz - \omega_L t)\,\hat{y}\right] \tag{4.1}$$

and

$$E_{\text{right}}(z,t) = \sqrt{2}E_0\left[\cos(kz + \omega_L t)\,\hat{x} - \sin(kz + \omega_L t)\,\hat{y}\right] \tag{4.2}$$

respectively, where $k = \omega_L/c$ is the wave number. Alternatively we can use

$$E_{\text{left}}(z,t) = E_0 e^{ikz - i\omega_L t}\hat{\epsilon}_{+1} + c.c. \tag{4.3}$$

and

$$E_{\text{right}}(z,t) = E_0 e^{ikz + i\omega_L t}\hat{\epsilon}_{-1} + c.c.\,, \tag{4.4}$$

where $\hat{\epsilon}_{\pm 1} = \mp(\hat{x} \pm i\hat{y})/\sqrt{2}$ are part of the spherical basis [see Eq. (4.12)]. The total laser electric field $E_L = E_{\text{left}} + E_{\text{right}}$ can be written in the form [23]

$$E_L(z,t) = E_+(z)e^{-i\omega_L t} + c.c. \tag{4.5}$$

where

$$E_+(z) = E_0\left[\sin(kz)\,\hat{x} + \cos(kz)\,\hat{y}\right] \tag{4.6}$$

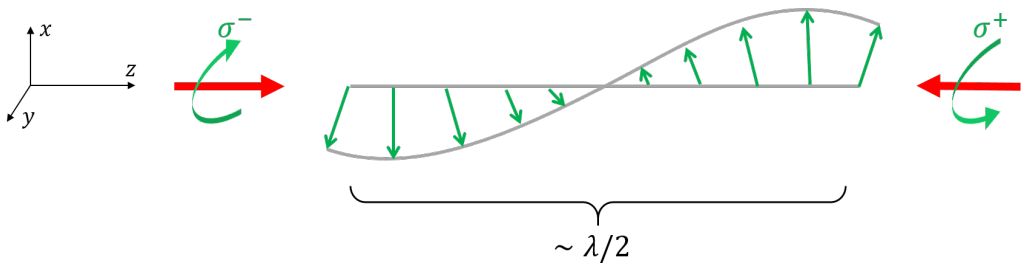

Figure 4.2: The $\sigma^+ - \sigma^-$ laser configuration leads to a locally linear polarization, but its direction depends on the position. After one wave length a full rotation is completed.

is the positive frequency component. This shows that the polarization at position z is linear but its direction changes as we move along the z-axis. After a full wave length λ it completes one full rotation. This position dependent polarization is illustrated in Fig. 4.2.

In order to deal with this configuration in our calculations we will transform into a spatially rotating frame. This is done by means of the unitary operator

$$\hat{T}(\theta) = \exp\left(-i\frac{\theta}{\hbar}\hat{J}_z\right), \tag{4.7}$$

where $\hat{J}_z$ is the z-component of the angular momentum operator and the generator of rotation around the z-axis. For the four states of the $J_g = 0 \to J_e = 1$ transition the action of $\hat{J}_z$ is given by

$$\hat{J}_z|e_m\rangle = \hbar m|e_m\rangle \quad \text{and} \quad \hat{J}_z|g\rangle = 0|g\rangle\ . \tag{4.8}$$

In the case at hand the angle of rotation $\theta = kz$ has an explicit time dependence due to the motion of the atom. Its position at time t is $z = z_0 + vt$ (we choose the origin such that $z_0 = 0$) and hence the angle is given by $\theta = kvt$. The change of basis operator becomes

$$\hat{T}(t) = \exp\left(-i\frac{kvt}{\hbar}\hat{J}_z\right). \tag{4.9}$$

As a consequence of this explicit time dependence the rotating frame is not inertial and the Hamiltonian will pick up an extra term given by [29]

$$V_{rot} = i\hbar\frac{d\hat{T}}{dt}\hat{T}^\dagger = kv\hat{J}_z\ . \tag{4.10}$$

4.1.3 The Hamiltonian and the Decay Term

Following the discussion for the evolution of the two-level atom (see Sec. 2.2), the full Hamiltonian can be reduced to an effective form given in Eq. (2.7) which is then

used in Eq. (2.6) to find the OBE. The first part of the Hamiltonian, i.e. H_A, is, using (2.15) to transfer into the temporal rotating frame,

$$H_A = \hbar\delta \sum_{m=0,\pm1} |e_m\rangle\langle e_m|. \tag{4.11}$$

For the second part (V_{AL}) we need to write the dipole operator analogues to Eq. (2.10), but now the vector nature of the dipole moment is important. Introducing the spherical basis

$$\hat{\epsilon}_{\pm1} = \mp\frac{\hat{x} \pm i\hat{y}}{\sqrt{2}} \quad , \quad \hat{\epsilon}_0 = \hat{z}. \tag{4.12}$$

the dipole operator is

$$\vec{d} = d_0 \left[C_{g\to e_{-1}}|e_{-1}\rangle\langle g|\hat{\epsilon}_{-1} + C_{g\to e_0}|e_0\rangle\langle g|\hat{\epsilon}_0 + C_{g\to e_{+1}}|e_{+1}\rangle\langle g|\hat{\epsilon}_{+1}\right] + h.c.\,, \tag{4.13}$$

where $C_{g\to e_m}$ are the Clebsch-Gordan coefficients given in Fig. 4.1. The first term is the σ^- transition, the second term the Π transition and the third term the σ^+ transition. The dipole operator can be written in a simplified form by defining the raising operators

$$\hat{A}_q^\dagger = C_{g\to e_q}|e_q\rangle\langle g|, \tag{4.14}$$

which, together with the lowering operators $\hat{A}_{-q}$, are represented in Fig. 4.3. We then simply have

$$\vec{d} = d_0 \sum_{q=0,\pm1} \hat{A}_q^\dagger \hat{\epsilon}_q + h.c., \tag{4.15}$$

where the summation index q can be interpreted as the photon polarization. A subtle point should be mentioned here. The *h.c.* of $\hat{A}_q^\dagger$ is $\hat{A}_{-q}$. (Note the minus sign in the subscript.) This is due to the fact that a photon with $q = +1$ is responsible for the transitions $|g\rangle \to |e_{+1}\rangle$ and $|e_{-1}\rangle \to |g\rangle$. In both cases the atomic angular momentum increases by $q = +1$ during the transition due to the absorption the photon. The interaction $V_{AL} = -\vec{d}\cdot\vec{E}_L$ is, using Eq. (4.13) for $\vec{d}$ and Eqs. (4.3) and (4.4) for $\vec{E}_L$,

$$V_{AL} = \hbar\Omega \left[C_{g\to e_{+1}}|e_{+1}\rangle\langle g|e^{ikz} + C_{g\to e_{-1}}|e_{-1}\rangle\langle g|e^{-ikz}\right] + h.c.\,, \tag{4.16}$$

where the Rabi frequency $\Omega = d_0E_0/\hbar$ is constant throughout space. Here we have already transformed into the temporal rotating frame. Note that the Π transition is not possible in the given setup [30].

The decay term γ_{dec} appearing in Eq. (2.6) is in general given by [13, 31]

$$\gamma_{dec} = \Gamma \sum_q A_q\rho(t)A_q^\dagger - \frac{\Gamma}{2}\sum_q \left(A_q^\dagger A_q\rho(t) + \rho(t)A_q^\dagger A_q\right). \tag{4.17}$$

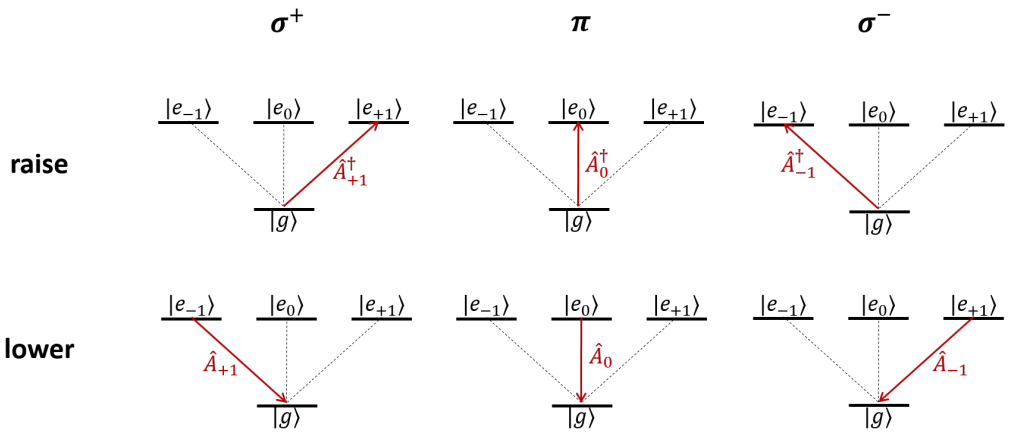

Figure 4.3: Graphic representation of the action of the three raising operators $\hat{A}_q^\dagger$ and their *h.c.*, $\hat{A}_{-q}$.

In the following the notation $\langle i|\rho|j\rangle = \rho(j,i)$ for the density matrix elements is used. For the excited state populations, Eq. (4.17) results in $\langle e_m|\gamma_{dec}|e_m\rangle = -\Gamma\rho(e_m,e_m)$. Their decay is therefore proportional to the population itself and to Γ. This could have been anticipated, noting that these terms just describe spontaneous emission. The excited state coherences behave in the same way: $\langle e_{m'}|\gamma_{dec}|e_m\rangle = -\Gamma\rho(e_m,e_{m'})$. The optical coherences decay half as fast, so $\langle g|\gamma_{dec}|e_m\rangle = -\Gamma/2\ \rho(e_m,g)$. The ground state population is fed by the decay of the excited states so $\langle g|\gamma_{dec}|g\rangle = +\Gamma\rho(e_{-1},e_{-1}) + \Gamma\rho(e_0,e_0) + \Gamma\rho(e_{+1},e_{+1})$. The only non-trivial terms are the ground state coherences but, since the ground state is non-degenerate, they do not exist here.

4.1.4 The Spatially Rotating Frame

The next step is to take the equation of motion, Eq. (2.6), and transform it into the spatially rotating frame by means of Eq. (4.9) [31]. This is not to be confused with the temporal rotating frame given by (2.15). The transformation leads to

$$\frac{d\rho_{rot}}{dt} = -\frac{i}{\hbar}\left[H_{rot}, \rho_{rot}(t)\right] + \gamma_{dec}, \tag{4.18}$$

where the density matrix in the rotating frame is

$$\rho_{rot} = \hat{T}\rho\hat{T}^\dagger \tag{4.19}$$

and the Hamiltonian

$$\begin{aligned} H_{rot} &= \hat{T}H\hat{T}^\dagger + i\hbar\frac{d\hat{T}}{dt}\hat{T}^\dagger \\ &= H_A^{(rot)} + V_{AL}^{(rot)} + V_{rot}\ . \end{aligned} \tag{4.20}$$

The decay term γ_{dec} remains invariant under the transformation. Using

$$\hat{T}|e_m\rangle\langle e_{m'}|\hat{T}^\dagger = e^{i(m'-m)kvt}|e_m\rangle\langle e_{m'}| \tag{4.21}$$

and

$$\hat{T}|e_m\rangle\langle g|\hat{T}^\dagger = e^{i(-m)kvt}|e_m\rangle\langle g| \tag{4.22}$$

we see right away that

$$H_A^{(rot)} = \hat{T}H_A\hat{T}^\dagger = H_A \tag{4.23}$$

and, using $z = vt$,

$$\begin{aligned} V_{AL}^{(rot)} = \hat{T}V_{AL}\hat{T}^\dagger &= \hbar\Omega\left[C_{g\to e_{+1}}|e_{+1}\rangle\langle g| + C_{g\to e_{-1}}|e_{-1}\rangle\langle g|\right] + h.c. \\ &= \hbar\Omega\left[A_{+1}^\dagger + A_{-1}^\dagger + h.c.\right]. \end{aligned} \tag{4.24}$$

Notice how conveniently the spatially rotating frame got rid of the z dependence in $V_{AL}^{(rot)}$. It follows that the Hamiltonian in the rotating frame is

$$H_{rot} = \hbar\delta\sum_{m=0,\pm1}|e_m\rangle\langle e_m| + \hbar\Omega\left[A_{+1}^\dagger + A_{-1}^\dagger + h.c.\right] + kv\hat{J}_z\ . \tag{4.25}$$

4.1.5 The Optical Bloch Equations

There are four atomic energy levels. This means that there are 16 OBE given by Eq. (4.18) in addition to the normalization condition $Tr\left(\rho_{rot}\right) = 1$. As for the two-level atom the density matrix can be written as a vector $\vec{\rho}$ and the coefficients as a 16×16 coefficient matrix $\overleftrightarrow{M}$. When the last row of $\overleftrightarrow{M}$ is switched for the normalization condition we obtain $\overleftrightarrow{M}_0$ and the steady state solution ρ_{rot}^{st} via Eq. (2.20).

4.1.6 The Force

A fundamental result of quantum mechanics is that the force operator $\hat{F}$ is given by the negative gradient of the Hamiltonian:

$$\hat{F} = -\nabla H. \tag{4.26}$$

In our case the only space dependent part is V_{AL} given by Eq. (4.16). After taking the derivative and transforming into the spatial rotating frame one gets

$$\hat{F}_{rot} = \hat{T}\hat{F}\hat{T}^\dagger = -i\hbar\Omega k\left[\hat{A}_{+1}^\dagger - \hat{A}_{-1}^\dagger\right] + h.c.\ . \tag{4.27}$$

The semi-classical force F is the average value of the force operator $\langle\hat{F}\rangle$ which is obtained by tracing over the steady state solution ρ^{st}. Although this is done in the

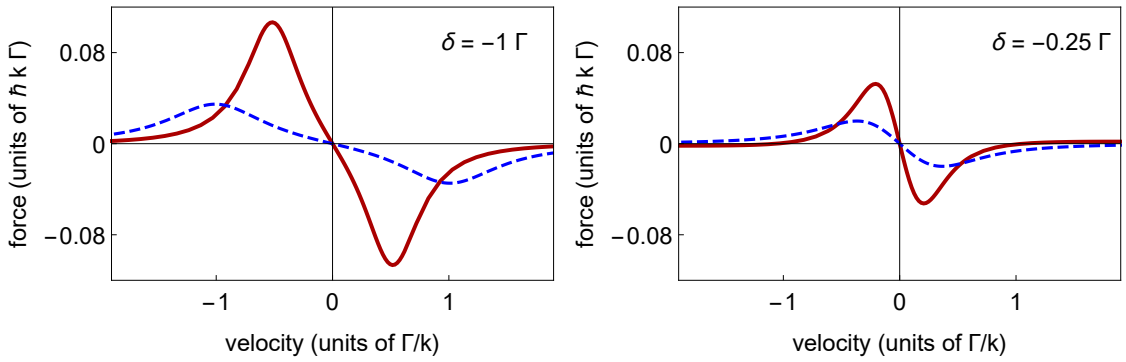

Figure 4.4: The force acting on the $J_g = 0 \rightarrow J_e = 1$ transition of an atom in a $\sigma^+ - \sigma^-$ laser configuration for $\delta = -\Gamma$ (left) and $\delta = -0.25\ \Gamma$ (right) (red solid). Here we used $\Omega = 0.2\ \Gamma$. For comparison the results for the two-level atom for the same parameters are shown blue dashed (taken from Fig. 2.2,).

rotating frame, using $\hat{F}_{rot}$ and ρ^{st}_{rot}, it is absolutely equivalent, since

$$\begin{aligned} \langle \hat{F} \rangle &= Tr\left(\hat{F}\rho^{st}\right) \\ &= Tr\left(\hat{F}\hat{T}^\dagger\hat{T}\rho^{st}\hat{T}^\dagger\hat{T}\right) = Tr\left(\hat{F}_{rot}\rho^{st}_{rot}\right) \end{aligned} \tag{4.28}$$

and one finds

$$\langle \hat{F} \rangle = 2\hbar k\Omega \times Im\left[\rho^{st}_{rot}\left(e_{+1}, g\right) + \rho^{st}_{rot}\left(e_{-1}, g\right)\right], \tag{4.29}$$

where we have used the fact that both relevant Clebsch-Gordan coefficients are equal to 1. This result has to be used twice. Once for the ρ^{st}_{rot} obtained by replacing $\delta \rightarrow \delta - kv$ (so $\vec{k} = +k\hat{z}$) and once for the ρ^{st}_{rot} obtained by replacing $\delta \rightarrow \delta + kv$ (so $\vec{k} = -k\hat{z}$). The two are then subtracted from one another and the total force shown in Fig. 4.4 is found.

Comparing this force to the one acting on a two-level atom (dashed line in Fig. 4.4) for the same parameters, we see that it is much stronger. The slope for $kv \ll \Gamma$ is much larger. One would therefore, a priori, expect a much lower steady state temperature. But of course nothing conclusive can be said before the diffusion coefficient is calcualted.

4.1.7 The Diffusion Coefficient

According to the FDT, a diffusion coefficient D intrinsically arises due to every force F. In general the relation is given by [5, 13]

$$\begin{aligned} D &= Re\left(\int d\tau \left\langle \delta F(t) \cdot \delta F(t-\tau) \right\rangle\right) \\ &= Re\left(\int d\tau \left[\left\langle F(t) \cdot F(t-\tau) \right\rangle - \left\langle F \right\rangle^2\right]\right), \end{aligned} \tag{4.30}$$

where $\delta F = F - \langle F \rangle$ is the fluctuation of the force around its mean value and the force operator is treated in the Heisenberg picture (it depends on time). Following the discussion above, the total diffusion coefficient $D = D^{vac} + D^{las}$ has two contributions. The one due to fluctuations in spontaneous emission, so D^{vac}, is the same as in Eq. (2.28) with the one slight change. Instead of ρ_{ee} we now must sum over all excited state populations, so

$$D^{vac} = \frac{1}{2}(\hbar k)^2 \sum_m \rho\left(e_m, e_m\right). \tag{4.31}$$

By quantizing the electromagnetic field and writting V_{AR} [see Eq. (2.1)] it can be shown rigorously that Eq. (4.30) leads to Eq. (4.31). The laser diffusion D^{las} is more complicated than in the simple two-level case. In particular, the assumption $D^{vac} \approx D^{las}$ is no longer true. We therefore have to take the proper approach and actually solve it. This means taking the laser force from Eq. (4.27) and plugging it into Eq. (4.30). For this we have to know how to evaluate one-time averages of the form $\langle \hat{A}_m^\dagger \rangle$ and two-time averages $\langle \hat{A}_q^\dagger(t) \hat{A}_{q'}(t-\tau) \rangle$. The one-time averages are simple. They just select a matrix element of ρ_{rot}^{st}:

$$\langle \hat{A}_q^\dagger \rangle = Tr\left(\hat{A}_q^\dagger \cdot \rho_{rot}^{st}\right) = C_{g \to e_q} \rho_{rot}^{st}\left(e_q, g\right). \tag{4.32}$$

For the two-time averages we have to work a little harder. First of all, only expressions with one raising and one lowering operator must be considered. Any other two-time average does not correspond a physical process and therefore must vanish. In addition, only part of the raise-lower (or lower-raise) processes work, namely, (consider Fig. 4.3):

- if the atom starts in $|g\rangle$

$$\langle \hat{A}_{+1}^\dagger(t) \hat{A}_{-1}(t-\tau) \rangle \quad \text{and} \quad \langle \hat{A}_{-1}^\dagger(t) \hat{A}_{+1}(t-\tau) \rangle, \tag{4.33}$$

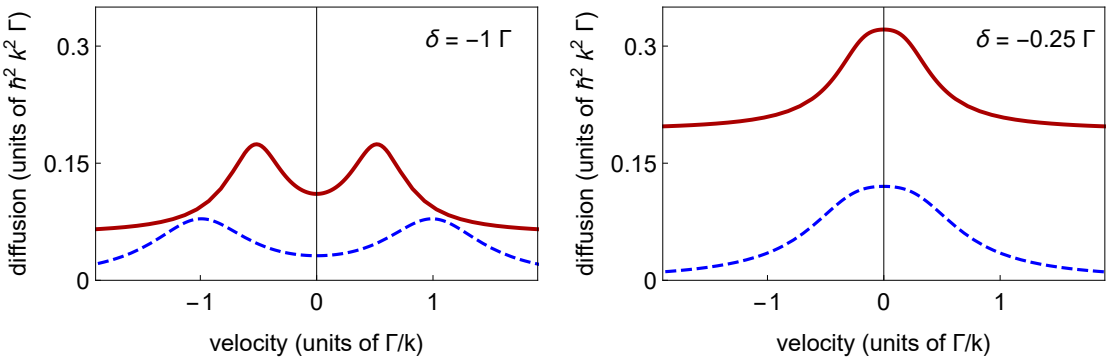

Figure 4.5: The diffusion coefficient felt by the $J_g = 0 \to J_e = 1$ transition of an atom in a $\sigma^+ - \sigma^-$ laser configuration for $\delta = -\Gamma$ (left) and $\delta = -0.25\ \Gamma$ (right) (red solid). Here we used $\Omega = 0.2\ \Gamma$. For comparison the line from Fig. 2.3 for the two-level atom is shown blue dashed.

- if it starts in $|e_{-1}\rangle$

$$\langle \hat{A}_{+1}(t)\hat{A}^{\dagger}_{-1}(t-\tau)\rangle \quad \text{and} \quad \langle \hat{A}_{+1}(t)\hat{A}^{\dagger}_{+1}(t-\tau)\rangle \tag{4.34}$$

- and if it starts in $|e_{+1}\rangle$

$$\langle \hat{A}_{-1}(t)\hat{A}^{\dagger}_{+1}(t-\tau)\rangle \quad \text{and} \quad \langle \hat{A}_{-1}(t)\hat{A}^{\dagger}_{-1}(t-\tau)\rangle. \tag{4.35}$$

The key for computing these averages is the quantum regression theorem (QRT) [14, 32]. It states that two-time averages evolve according to the same equations as the one-time averages, i.e. according to the OBE. In general, in order to calculate the two time average $\langle \hat{A}(t)\hat{B}(t-\tau)\rangle$ one must first find the reduced density matrix $\rho^A(\tau)$ by solving the differential equation

$$\frac{d}{d\tau}\vec{\rho}^A = \overleftrightarrow{M} \cdot \vec{\rho}^A(\tau) \tag{4.36}$$

subject to the initial conditions $\rho^A(0) = \hat{A} \cdot \rho^{st}$. The two-time average is then found by taking the trace

$$\langle \hat{A}(t)\hat{B}(t-\tau)\rangle = Tr\left(\hat{B} \cdot \rho^A(\tau)\right). \tag{4.37}$$

Doing so for all six non-zero two-time averages and plugging them into Eq. (4.30) together with Eq. (4.32) leads to D^{las}.

The total diffusion coefficient $D = D^{vac} + D^{las}$ is shown in Fig. 4.5. As already seen for the force, also the diffusion coefficient is larger than for the two-level atom. The increased force is accompanied by an increased diffusion.

Another feature on the diffusion coefficient seen in Fig. 4.5 is that it does not fall of to zero for large velocities. Instead it approaches a constant value. This is a

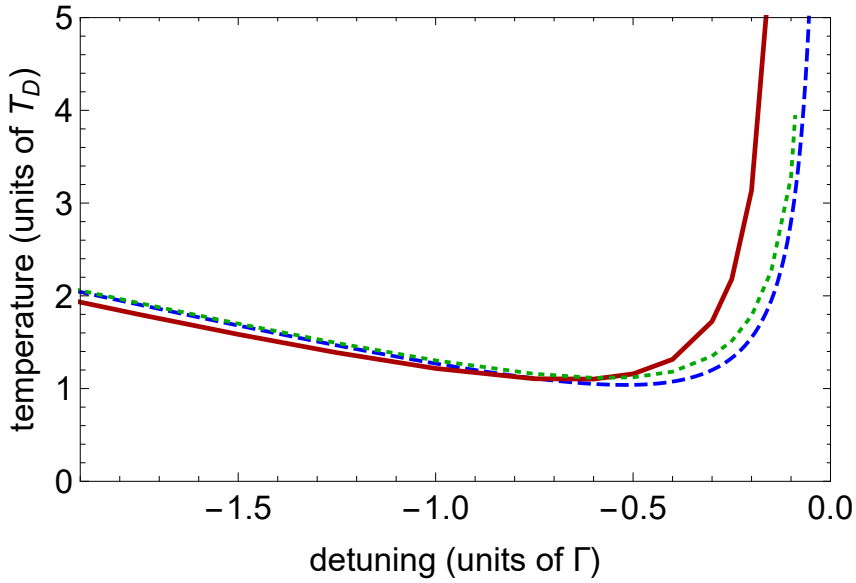

Figure 4.6: A plot of the temperature as a function of detuning for $\Omega = 0.2\ \Gamma$. The green dotted line is obtained via the FDT (method 1) and the red solid line by numerically integrating Eq. (2.36) and fitting to a Gaussian (method 2). For comparison the simple two-level theory given by Eq. (2.33) is shown blue dashed.

by product of the transformation to a spatially rotating frame which is applicable only in the low velocity limit ($kv \ll \Gamma$). The actual diffusion coefficient vanishes for growing velocity.

4.1.8 The Temperature

Referring to Sec. 2.6 there are two methods for finding the temperature. The first is based on approximating the force to $F \approx -\alpha v$, where α is the friction coefficient, and the diffusion coefficient to $D(v) \approx D(0)$. By means of the FDT [Eq. (2.32)] the temperature is computed, plotted green dotted in Fig. 4.6 and found to be almost equal to the two-level temperature given in Eq. (2.33).

The second method utilizes the FP equation. The force $F(v)$ and the diffusion coefficient $D(v)$ are plugged into Eq. (2.36) to obtain the velocity distribution $W(v)$. Since we do not have analytical expressions for $F(v)$ and $D(v)$ the integral is solved numerically. Note that only the ratio $F(v)/D(v)$ enters the exponential function in Eq. (2.36) and so the fact that $D(v)$ does not vanish for large velocities does not prevent convergence of $W(v)$. Due to the vanishing of the force, i.e. $F(v \to \infty) \to 0$, the integral will do so as well and the obtained velocity distribution behaves normally. Although for $k|v| \gtrsim \Gamma$ the calculated distribution might deviate from the actual distribution due to the limit of validity of the spatially rotating frame. The obtained distribution is fitted to a Gaussian using the width $\langle v^2 \rangle$ as a fitting parameter which is translated to temperature by means of the first equality in Eq. (2.38).

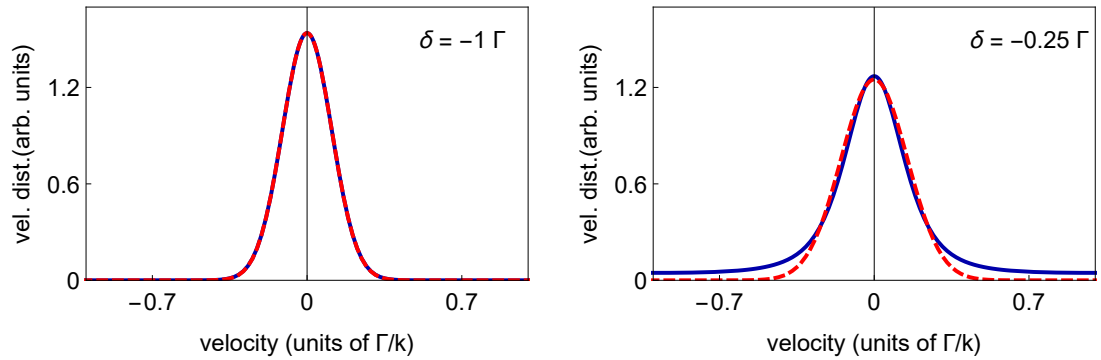

Figure 4.7: The velocity distribution $W(v)$ is shown as a function of the atomic velocity as a blue solid line for $\delta = -\Gamma$ (left) and $\delta = -0.25\ \Gamma$ (right). The Gaussian fit is shown dashed.

In Fig. 4.7 the calculated distribution is shown together with a Gaussian fit for different values of the detuning. As the detuning approaches resonance ($\delta \to 0$) the real distribution becomes less Gaussian. We therefore rediscover the phenomenon already pointed out when discussing the exact solution and the FP approach for the two-level atom.

The temperature is plotted versus the detuning in Fig. 4.6 and compared to the simple two-level atom. For $\delta \lesssim 0.5\ \Gamma$, the region for which $W(v)$ is Gaussian, the same result as for the simple two level system is obtained. So, although the force is stronger, the diffusion coefficient is larger by just the right amount to exactly compensate this increase and the steady state temperature is unchanged. In the regime of non-Gaussian distributions, $\delta > -0.5\ \Gamma$, a discrepancy with the simple two -level theory is found. However, *because* the distribution is non-Gaussian, the values obtained for the temperature must be treated with extra care.

As an experimental example for the $J_g = 0 \to J_e = 1$ transition, see the bosonic isotopes of mercury shown in Fig. 2.6, where agreement with a two-level atom is shown.

4.2 The $J_g = 1 \to J_e = 2$ Transition

4.2.1 The Set-Up

A more interesting atomic system is the $J_g = 1 \to J_e = 2$ transition shown in Fig. 4.8. It has three degenerate ground states $|g_m\rangle$ and five degenerate excited states $|e_m\rangle$. The procedure described above for the $J_g = 0 \to J_e = 1$ transition in a $\sigma^+ - \sigma^-$ laser configuration can be directly applied. The generalization introduces no new mathematical concepts and will therefore not be further discussed here. Just note that the raising operators given in Eq. (4.14) now include a sum over all σ^+

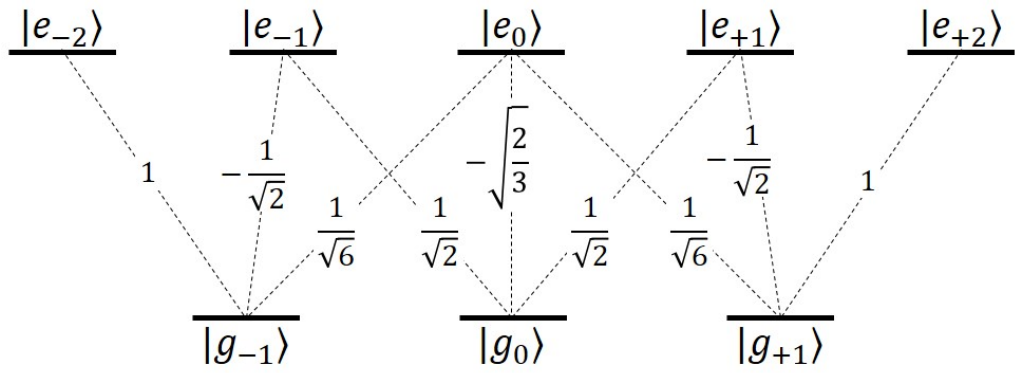

Figure 4.8: The eight atomic levels (three ground states and five excited states) of the $J_g = 1 \rightarrow J_e = 2$ transition. The Clebsch-Gordan coefficents of the allowed dipole transitions are shown.

($q = 1$), σ^- ($q = -1$) or Π ($q = 0$) transitions, where q is the spin state of the photon:

$$\hat{A}_q^\dagger = \sum_m C_{g_m \rightarrow e_{m+q}} |e_{m+q}\rangle\langle g_m|. \tag{4.38}$$

The Clebsch-Gordan coefficients $C_{g_m \rightarrow e_{m+q}}$ are indicated in Fig. 4.8 and, also here, the *h.c.* of $\hat{A}_q^\dagger$ is $\hat{A}_{-q}$.

4.2.2 The Force and Diffusion Coefficient

Instead of going over the mathematical procedure we jump straight to the results and focus on the physical interpretation. The fact that not only the excited state, but also the ground state is degenerate gives rise to the possibility of so-called sub-Doppler cooling, as we shall see.

Fig. 4.9 shows the force $F(v)$ as a red solid line. Although it more or less coincides with the $J_g = 0 \rightarrow J_e = 1$ force (green dotted), its slope makes an abrupt change and becomes much steeper as $v \rightarrow 0$. If an atom can be brought to the relevant velocities it will experience a very strong cooling force. This increased friction is due to a very different mechanism than Doppler cooling [23].

Since the local polarization is linear [see Eq. (4.6)] and its direction, because of the spatial rotating frame, constant in space the polarization axis is best chosen to be along $\hat{y}$ [plug $z = 0$ into Eq. (4.6)]. The ground state eigenstates are denoted $|g_m\rangle_y$ in this basis. A light-shift (or AC-Stark shift) that is proportional to the $q = 0$ transition is then introduced. From the Clebsch-Gordan coefficients in Fig. 4.8 it is obvious that it is larger for $|g_0\rangle_y$ than for $|g_{\pm 1}\rangle_y$. The additional term in the Hamiltonian given in Eq. (4.10) can be treated perturbatively in the limit where kv is much smaller than this light-shift. Although the numerical calculations presented here are not limited to small velocities, we can get a lot of insight from such a

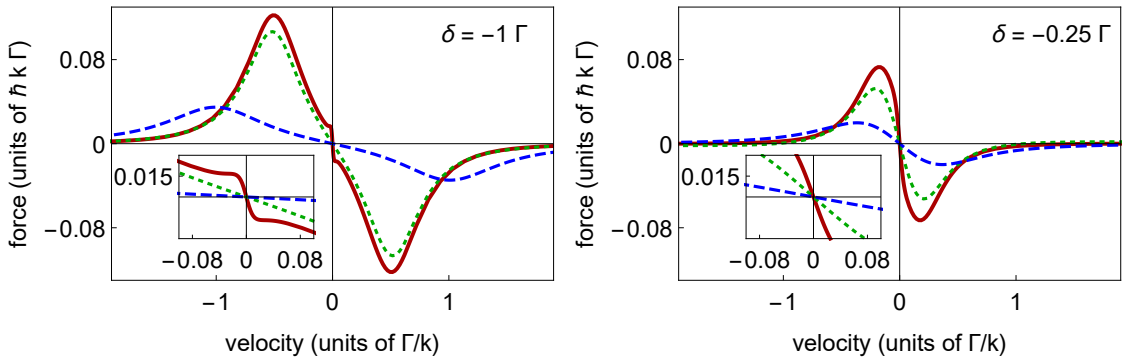

Figure 4.9: The force acting on the $J_g = 1 \to J_e = 2$ transition of an atom in a $\sigma^+ - \sigma^-$ laser configuration for $\delta = -\Gamma$ (left) and $\delta = -0.25\ \Gamma$ (right) (red solid). Here we used $\Omega = 0.2\ \Gamma$. For comparison, the results for two-level atom (blue dashed) and for the $J_g = 0 \to J_e = 1$ transition (green dotted) are shown for the same parameters.

treatment especially since the increased force appears precisely in this limit, as is apparent from Fig. 4.9. The angular momentum operator $\hat{J}_z$ appearing in Eq. (4.10) will mix the $|g_m\rangle_y$ states when first order perturbation theory is performed. If we then take the average $\langle \hat{J}_z \rangle$ we discover that it is non-zero, as it would be for $v = 0$, meaning that the $|g_{\pm 1}\rangle_z$ states (in the eigenbasis of $\hat{J}_z$) are not populated equally. One can show that for $\vec{v} = +v\hat{z}$ the state $|g_{+1}\rangle_z$ is more populated than $|g_{-1}\rangle_z$. Hence the atom will absorb σ^+ photons, which are coming from the right and counter-propagating the atom, with a higher probability than the co-propagating σ^- photons, causing an increased cooling force. We stress that this cooling mechanism is due to the population imbalance introduced by Eq. (4.10) and not due to the Doppler shift. As can be seen in Fig. 4.9, this increased cooling force is limited to very low velocities. So by defining the sub-Doppler capture velocity v_c below which this new mechanism can work we have

$$\frac{kv_c}{\Gamma} \ll 1. \tag{4.39}$$

The cooling mechanism active for $v > v_c$, and therefore the mechanism that can reduce v to the threshold v_c, is regular Doppler cooling. Hence, if the Doppler velocity $v_D = \sqrt{\hbar\Gamma/m}$, which is the velocity of an atom at the Doppler limit, is on the order of or below v_c, sub-Doppler cooling can start working. Otherwise, although the strong increase in the slope of the force is present, the atoms will never reach the required v_c. The condition is thus

$$\frac{kv_D}{\Gamma} = \sqrt{\frac{2\omega_r}{\Gamma}} \ll 1, \tag{4.40}$$

where $\omega_r = \hbar k^2/2m$ is the recoil frequency associated with the single photon recoil

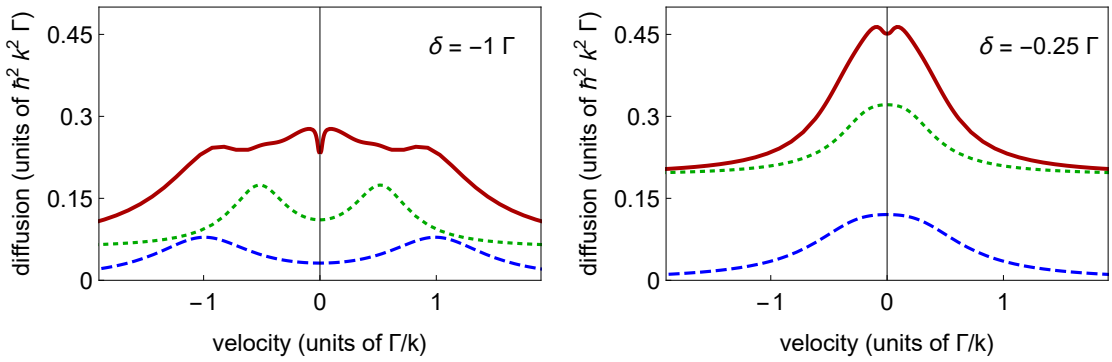

Figure 4.10: The diffusion coefficient felt by the $J_g = 1 \to J_e = 2$ transition of an atom in a $\sigma^+ - \sigma^-$ laser configuration for $\delta = -\Gamma$ (left) and $\delta = -0.25\ \Gamma$ (right) (red solid). Here we used $\Omega = 0.2\ \Gamma$. For comparison, the results for two-level atom (blue dashed) and for the $J_g = 0 \to J_e = 1$ transition (green dotted) are shown for the same parameters.

energy $E_r = \hbar\omega_r$.

The diffusion coefficient, shown in Fig. 4.10, is larger than for the previously discussed cases. This can be explained by optical pumping [23, 33]. After an atom absorbs, say, a σ^+ photon it is more likely to absorb another one of the same type than a σ^- photon. This means that the step size Δp is larger than the single photon momentum $\hbar k$ causing the diffusion coefficient to be larger. Also here, as $v \to 0$ sub-Doppler features appear due to the motion-induced population imbalance.

4.2.3 The Temperature

Again, there are two options to compute the temperature (see Sec. 2.6). But now, because of the sub-Doppler features, the two treatments lead to very different results, both of which are presented here. The criterion for deciding which method to use is the ratio v_D/v_c. The suitability of each method thus depends on atomic parameters [see Eq. (4.40)], namely ω_r and Γ.

Following the first method, the force is expanded up to first order, so $F \approx -\alpha v$, and the diffusion coefficient approximated by the constant value $D(v) \approx D(0)$. This treatment is valid in the case where $v_D < v_c$, so when the sub-Doppler capture velocity is reached by Doppler cooling. By means of Eq. (2.32) the temperature is obtained. Due to the strongly increased slope of the force this leads to temperatures way below the Doppler limit, as can be seen in Fig. 4.11, and hence this mechanism is called sub-Doppler cooling. One sees that, despite the increase of the diffusion, which is due to optical pumping introduced by the degenerate ground state, the force is so much stronger that it more than compensates this extra heating.

If $v_D > v_c$ a linearization of the force is not possible and one must resolve to the second option, which is to plug $F(v)$ and $D(v)$ as is into Eq. (2.36) to obtain

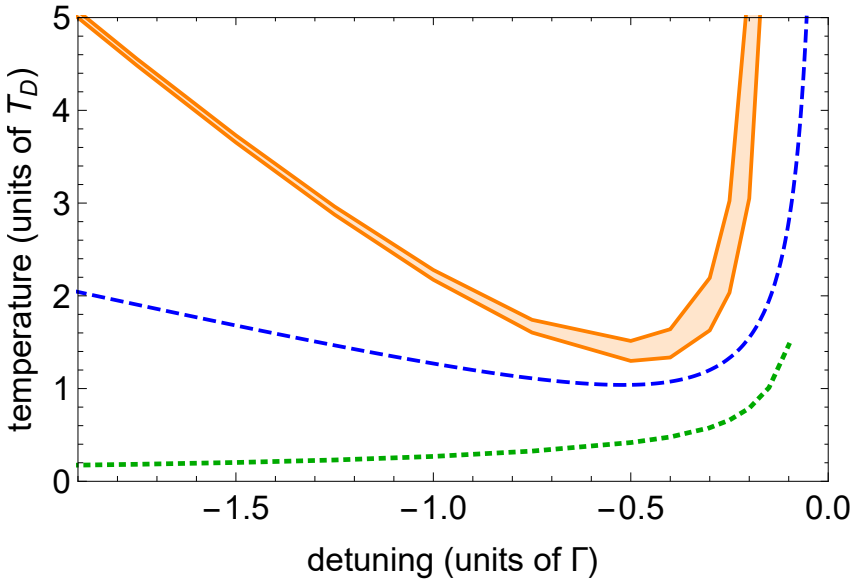

Figure 4.11: A plot of the temperature as a function of detuning for $\Omega = 0.2\ \Gamma$. The orange region is obtained by numerically integrating Eq. (2.36) and fitting the non-sub-Doppler velocities to a Gaussian. Alternatively, the green dotted line is obtained by expanding the force to first and the diffusion coefficient to zeroth order around $v = 0$. For comparison the simple two-level theory, given by Eq. (2.33), is shown dashed.

$W(v)$. The result is shown in Fig. 4.12. Note how the sub-Doppler features effect the velocity distribution around $v = 0$. In a 1D model, which is what we are dealing with, the $v = 0$ state is the most probable. But in the three dimensional (3D) experiment this is not the case. According to 3D Maxwell-Boltzmann statistics the velocity $v = |v|$ only takes positive values. The most probable velocity is $\sqrt{2k_BT/m}$ and the average and standard deviation are

$$\langle v \rangle = \sqrt{\frac{8k_BT}{\pi m}} \quad \text{and} \quad \sqrt{\langle v^2 \rangle} = \sqrt{\frac{3k_BT}{m}} \tag{4.41}$$

respectively. The probability to be at $v \approx 0$ is vanishingly small. In order to encorporate this in our 1D model we must cast away these unrealistic velocities. Hence, when fitting $W(v)$ to a Gaussian, only the points outside the sub-Doppler region are used. This region cannot be determined precisely so the fitting procedure is repeated for different ignored velocity ranges. In Fig. 4.12 two example distributions are plotted together with their fits without the regions $k|v|/\Gamma < 0.04$ (smallest ignored range) and $k|v|/\Gamma < 0.08$ (largest ignored range). From the width $\langle v^2 \rangle$ of the different fits an estimation interval for the temperature is obtained via the first equality in Eq. (2.38) and the result is plotted in Fig. 4.11 as a function of the detuning (orange region). The higher (lower) solid line is the maximal (minimal) prediction which corresponds to the largest (smallest) ignored velocity range

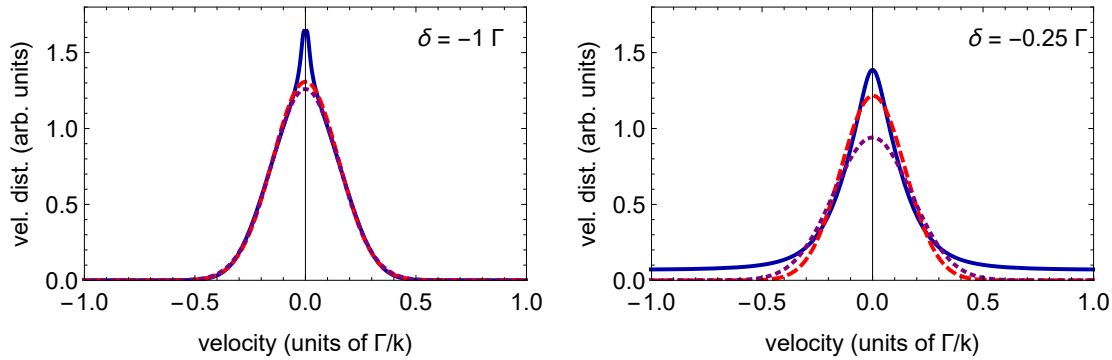

Figure 4.12: The velocity distribution $W(v)$ is shown as a function of the atomic velocity as a blue solid line for $\delta = -\Gamma$ (left) and $\delta = -0.25\ \Gamma$ (right). The red dashed and purple dotted lines are Gaussian fits to $W(v)$ without the points for $|v| < 0.04\ \Gamma/k$ and $|v| < 0.08\ \Gamma/k$ respectively.

$k|v|/\Gamma < 0.08$ ($k|v|/\Gamma < 0.04$). The extra heating coming from the increased diffusion coefficient is well expressed for $\delta < -0.5\ \Gamma$ although, for $\delta \approx -0.5\ \Gamma$ the force is still strong enough for the temperature to almost reach the Doppler limit. For $\delta > -0.5\ \Gamma$ the prediction deviates from the simple two-level atom and the temperature diverges much sooner. But the prediction is less trustworthy in this region since the distribution is more non-Gaussian as can be seen in Fig. 4.12. This non-Gaussianity also causes the orange region in Fig. 4.11 to be wider as $\delta \to 0$.

4.3 Multi-Level Atom

We have come a far way. The two-level atom is well understood and its predictions, namely the Doppler limit $k_B T_D = \hbar\Gamma/2$ and the divergence for $\delta \to 0$, known. Also the effect of a degenerate ground-state, and how it makes sub-Doppler temperatures reachable, is a familiar subject. In addition we have seen that if the Doppler velocity is above the capture velocity of sub-Doppler cooling, no sub-Doppler cooling occurs and the irrelevant region ($|v| < v_c$) must not be considered in the 1D analyses.

But real atoms have far more than two levels. Besides Zeeman sub-levels, which were introduced and discussed in the previous sections, there is hyper-fine splitting which arises due to the coupling of the orbital angular momentum L with the electron spin S and the nuclear spin I. In this section we will explore the physics involved in such a rich and complicated system. The goal is to quantitatively describe the results of the experiment presented in Sec. 3.3.1.

4.3.1 The Multi-Level Structure of Lithium

In the case of ^{7}Li, shown in Fig. 3.1, we have electron spin $S = 1/2$ (hydrogen like, i.e. one valence electron) and nuclear spin $I = 3/2$. The ground state, for which $L = 0$, has two distinct energy levels: $|F = 1\rangle$ and $|F = 2\rangle$. In the excited state ($L = 1$) all four values $|F' = 0, 1, 2, 3\rangle$ appear. We use an unprimed $|F\rangle$ to denote a ground state and a primed $|F'\rangle$ to denote an excited state when it is necessary to distinguish. In addition to the hyper-fine splitting each level is $(2F + 1)$-fold degenerate due to the Zeeman sub-levels. The total number of states is a dazzling 24! In the calculation presented here we spare no effort and take all of them into account.

A few points should be noted:

1. The energy difference in the gound state is large ($\sim 136\ \Gamma$). Hence, two lasers with a distinct frequency must be used. The one starting from $|F = 2\rangle$ is called pump and the other, starting at $|F = 1\rangle$, repump. They are shown in Fig. 3.1 together with the allowed dipole transitions.

2. Unlike the ground state, the four excited levels are energetically very close ($\sim \Gamma$). This makes all four levels easily accessible and all four will be populated.

3. Take a close look at the excited states. The order is inversed. The lowest energy level is $|F' = 3\rangle$ while the highest one is $|F' = 0\rangle$. This feature is not unique to ^{7}Li but it is rare. (Another example is ^{40}K.) Since $|F = 2\rangle \rightarrow |F' = 3\rangle$ is the strongest transition, the pump detuning δ_p is measured relative to it. Hence, if it is set to resonance, so $\delta_p = 0$, the remaining two levels $|F' = 2, 1\rangle$ remain red detuned. This is the necessary condition for Doppler cooling and therefore offers a hand-waving argument for the possibility of cooling at $\delta_p = 0$. But this is only the beginning of the story.

4. The repump detuning δ_r is also measured relative to its strongest transition, namely $|F = 1\rangle \rightarrow |F' = 2\rangle$. Also here the remaining to levels are red detuned at $\delta_r = 0$.

4.3.2 Setting Up the Optical Bloch Equations

The Hamiltonian

The system involves two lasers, called pump and repump, with distinct frequencies ω_p and ω_r respectively. As in the experiment the detuning of the repump is set to $\delta_r = 0$ during the entire analyses. The Hamiltonian includes two parts: one for

$\|F'\rangle$	$\Delta_{F'}$ pump	$\Delta_{F'}$ repump
3	0	forbidden
2	1.56 Γ	0
1	2.61 Γ	1.05 Γ
0	forbidden	1.58 Γ

Table 4.1: The frequency of the pump (repump) laser is measured with respect to the $|F' = 3\rangle$ ($|F' = 2\rangle$) excited state. The other states are additionally detuned from it. The frequency $\Delta_{F'}$ is the additional detuning of the state $|F'\rangle$.

the pump (H_p) and one for the repump (H_r). In addition there is a term, given by Eq. (4.10), due to the rotating frame. We have

$$H_{rot} = H_p^{(rot)} + H_r^{(rot)} + V_{rot}. \tag{4.42}$$

The first two parts take the form of Eq. (2.7), so, for the pump

$$H_p^{(rot)} = H_A^{(p)(rot)} + V_{AL}^{(p)(rot)}. \tag{4.43}$$

Here the pump laser is discussed in detail. The repump can be treated equivalently.

The absolute detuning of the pump δ_p is measured with respect to the main transition, namely $|F = 2\rangle \rightarrow |F' = 3\rangle$. The selection rules also allow the dipole transitions $|F = 2\rangle \rightarrow |F' = 2\rangle$ and $|F = 2\rangle \rightarrow |F' = 1\rangle$ but the transition $|F = 2\rangle \rightarrow |F' = 0\rangle$ is forbidden. The detuning of the level $|F'\rangle$ is

$$\delta_{F'}^{(p)} = \delta_p - \Delta_{F'}, \tag{4.44}$$

where $\Delta_{F'}$ is given in Table 4.1. The atomic part of the pump Hamiltonian is thus

$$H_A^{(p)} = \hbar \sum_{F', m_{F'}} \delta_{F'}^{(p)} |F', m_{F'}\rangle\langle F', m_{F'}|, \tag{4.45}$$

where $\delta_{F'}^{(p)}$ is given by Eq. (4.44) and we have already made the transformation into the temporal rotating frame [see Eq. (2.15)]. The spatial rotating frame leaves $H_A^{(p)}$ untouched and so $H_A^{(p)(rot)} = H_A^{(p)}$.

The interaction term of the pump Hamiltonian, $V_{AL}^{(p)}$, consists of the dipole moment $\vec{d}^{(p)}$ for the pump transitions (see Fig. 3.1, the ones starting at $|F = 2\rangle$) and the pump laser electric field $\vec{E}_p$, and is given by Eq. (2.9). The dipole moment is

$$\vec{d}^{(p)} = d_0^{(p)} \sum_{q=0,\pm1} \left(\hat{A}_q^{(p)}\right)^\dagger \hat{\epsilon}_q + h.c.\ , \tag{4.46}$$

		$\|F=2\rangle$				
		$\|m_F=-2\rangle$	$\|m_F=-1\rangle$	$\|m_F=0\rangle$	$\|m_F=+1\rangle$	$\|m_F=+2\rangle$
$\|F'=0\rangle$	$\|m_{F'}=0\rangle$	0	0	0	0	0
$\|F'=1\rangle$	$\|m_{F'}=-1\rangle$	$\frac{1}{\sqrt{10}}$	$\frac{1}{\sqrt{20}}$	$\frac{1}{\sqrt{60}}$	0	0
	$\|m_{F'}=0\rangle$	0	$\frac{1}{\sqrt{20}}$	$\frac{1}{\sqrt{15}}$	$\frac{1}{\sqrt{20}}$	0
	$\|m_{F'}=+1\rangle$	0	0	$\frac{1}{\sqrt{60}}$	$\frac{1}{\sqrt{20}}$	$\frac{1}{\sqrt{10}}$
$\|F'=2\rangle$	$\|m_{F'}=-2\rangle$	$-\frac{1}{\sqrt{3}}$	$-\frac{1}{\sqrt{6}}$	0	0	0
	$\|m_{F'}=-1\rangle$	$\frac{1}{\sqrt{6}}$	$\frac{1}{\sqrt{12}}$	$-\frac{1}{2}$	0	0
	$\|m_{F'}=0\rangle$	0	$\frac{1}{2}$	0	$-\frac{1}{2}$	0
	$\|m_{F'}=+1\rangle$	0	0	$\frac{1}{2}$	$\frac{1}{\sqrt{12}}$	$-\frac{1}{\sqrt{6}}$
	$\|m_{F'}=+2\rangle$	0	0	0	$\frac{1}{\sqrt{6}}$	$\frac{1}{\sqrt{3}}$
$\|F'=2\rangle$	$\|m_{F'}=-3\rangle$	1	0	0	0	0
	$\|m_{F'}=-2\rangle$	$-\frac{1}{\sqrt{3}}$	$\sqrt{\frac{2}{3}}$	0	0	0
	$\|m_{F'}=-1\rangle$	$\frac{1}{\sqrt{15}}$	$-\sqrt{\frac{8}{15}}$	$\sqrt{\frac{2}{5}}$	0	0
	$\|m_{F'}=0\rangle$	0	$\frac{1}{\sqrt{5}}$	$-\sqrt{\frac{3}{5}}$	$\frac{1}{\sqrt{5}}$	0
	$\|m_{F'}=+1\rangle$	0	0	$\sqrt{\frac{2}{5}}$	$-\sqrt{\frac{8}{15}}$	$\frac{1}{\sqrt{15}}$
	$\|m_{F'}=+2\rangle$	0	0	0	$\sqrt{\frac{2}{3}}$	$-\frac{1}{\sqrt{3}}$
	$\|m_{F'}=+3\rangle$	0	0	0	0	1

Table 4.2: The Clebsch-Gordan coefficients of the pump transitions of the D_2-line of ^{7}Li shown in Fig. 3.1.

which is equivalent to Eq. (4.15), and where the raising operators are

$$\left(\hat{A}_q^{(p)}\right)^\dagger = \sum_{F'} \sum_{m_F=-2}^{2} C_{(F',m_F+q;2,m_F)} \left|F', m_F+q\right\rangle\left\langle 2, m_F\right|, \tag{4.47}$$

equivalent to Eq. (4.38). The $C_{(F',m_{F'};F,m_F)}$ are the Clebsch-Gordan coefficients for the pump transitions given in Table 4.2. The electric field of the pump laser is

$$\vec{E}_p = E_0^{(p)}\left[e^{ikz-i\omega_p t}\hat{\epsilon}_{+1} + e^{ikz+i\omega_p t}\hat{\epsilon}_{-1}\right] + c.c. \tag{4.48}$$

in agreement with Eqs. (4.3) and (4.4). According to Eq. (2.9) and using Eqs. (2.15) and (4.9) to transform into both the temporal and spatial rotating frames, the interaction term is

$$V_{AL}^{(p)(rot)} = \hbar\Omega_p \sum_{q=\pm1} \sum_{F'=1,2,3} \sum_{m_F=-2}^{2} C_{(F',m_F+q;2,m_F)} \left|F', m_F+q\right\rangle\left\langle 2, m_F\right| + h.c., \tag{4.49}$$

where $\Omega_p = -d_0^{(p)}E_0^{(p)}/\hbar$ is the Rabi frequency of the pump laser.

For the repump laser one obtains

$$H_A^{(r)} = \hbar \sum_{F',m_{F'}} \delta_{F'}^{(r)} |F', m_{F'}\rangle\langle F', m_{F'}|, \tag{4.50}$$

		$\|F=1\rangle$		
		$\|m_F=-1\rangle$	$\|m_F=0\rangle$	$\|m_F=+1\rangle$
$\|F'=0\rangle$	$\|m_{F'}=0\rangle$	$\frac{1}{\sqrt{3}}$	$\frac{1}{\sqrt{3}}$	$\frac{1}{\sqrt{3}}$
$\|F'=1\rangle$	$\|m_{F'}=-1\rangle$	$-\sqrt{\frac{5}{12}}$	$-\sqrt{\frac{5}{12}}$	0
	$\|m_{F'}=0\rangle$	$\sqrt{\frac{5}{12}}$	0	$-\sqrt{\frac{5}{12}}$
	$\|m_{F'}=+1\rangle$	0	$\sqrt{\frac{5}{12}}$	$\sqrt{\frac{5}{12}}$
$\|F'=2\rangle$	$\|m_{F'}=-2\rangle$	$\frac{1}{\sqrt{2}}$	0	0
	$\|m_{F'}=-1\rangle$	$-\frac{1}{2}$	$\frac{1}{2}$	0
	$\|m_{F'}=0\rangle$	$\frac{1}{\sqrt{12}}$	$-\frac{1}{\sqrt{3}}$	$\frac{1}{\sqrt{12}}$
	$\|m_{F'}=+1\rangle$	0	$\frac{1}{2}$	$-\frac{1}{2}$
	$\|m_{F'}=+2\rangle$	0	0	$\frac{1}{\sqrt{2}}$
$\|F'=2\rangle$	$\|m_{F'}=-3\rangle$	0	0	0
	$\|m_{F'}=-2\rangle$	0	0	0
	$\|m_{F'}=-1\rangle$	0	0	0
	$\|m_{F'}=0\rangle$	0	0	0
	$\|m_{F'}=+1\rangle$	0	0	0
	$\|m_{F'}=+2\rangle$	0	0	0
	$\|m_{F'}=+3\rangle$	0	0	0

Table 4.3: The Clebsch-Gordan coefficients of the repump transitions of the D_2-line of ^{7}Li shown in Fig. 3.1.

where $\delta_{F'}^{(r)} = \Delta_{F'}$ (remember that $\delta_r = 0$) and $\Delta_{F'}$ is given in Table 4.1, and

$$V_{AL}^{(r)(rot)} = \hbar\Omega_r \sum_{q=\pm1} \sum_{F'=0,1,2} \sum_{m_F=-1}^{1} C_{(F',m_F+q;1,m_F)} \left|F', m_F+q\right\rangle\left\langle 1, m_F\right| + h.c., \quad (4.51)$$

where the Clebsch-Gordan coefficients for the repump transitions are given in Table 4.3. Together, Eqs. (4.50) and (4.51) form the repump Hamiltonian

$$H_r^{(rot)} = H_A^{(r)(rot)} + V_{AL}^{(r)(rot)}. \quad (4.52)$$

Finally, the repump raising operator is given by

$$\left(\hat{A}_q^{(r)}\right)^\dagger = \sum_{F'} \sum_{m_F=-1}^{1} C_{(F',m_F+q;1,m_F)} \left|F', m_F+q\right\rangle\left\langle 1, m_F\right|. \quad (4.53)$$

We now turn to the decay term γ_{dec} appearing in Eq. (4.18). As in Eq. (4.17) it can be expressed neatly by means of the raising operators and their *h.c.*, the lowering operators. But here the raising operator is the sum of the pump raising operator [Eq. (4.47)] and the repump raising operator [Eq. (4.53)], i.e.

$$A_q^\dagger = \left(\hat{A}_q^{(p)}\right)^\dagger + \left(\hat{A}_q^{(r)}\right)^\dagger. \quad (4.54)$$

Using this definition Eq. (4.17) can be readily used.

Everything needed is ready. All that is left to do is to collect the bits and

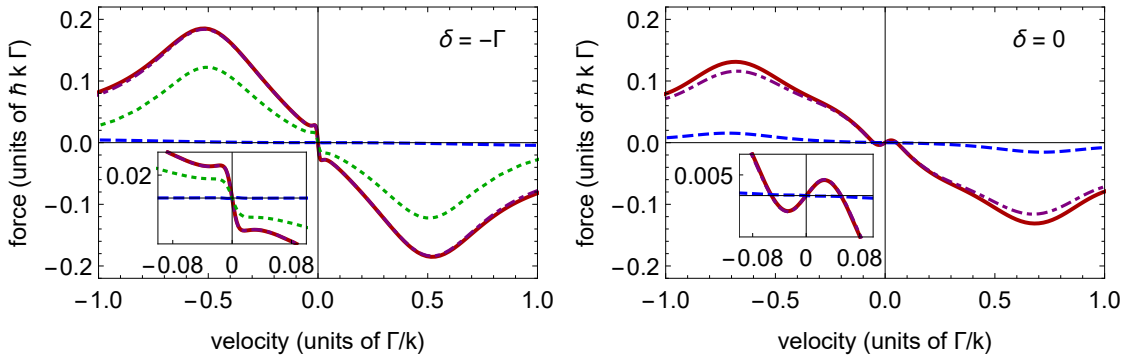

Figure 4.13: The force acting on a ^{7}Li atom in a $\sigma^+ - \sigma^-$ laser configuration for $\delta = -\Gamma$ (left) and $\delta = 0$ (right) (red solid). Here we used $\Omega_p = 0.26\ \Gamma$ and $\Omega_r = 0.4\ \Gamma$. For comparison, the force for the $J_g = 1 \rightarrow J_e = 2$ transition from Fig. 4.9 is shown green dotted in the left plot. The purple dot-dashed and and blue dashed lines show the contributions of the pump and repump laser respectively.

pieces and plug them into Eq. (4.18). We then follow the procedure presented in Sec. 2.3, which includes writing a coefficient matrix $\overleftrightarrow{M_0}$ and taking its inverse, to find the steady state solution ρ^{st}_{rot}. In the following sections the results of the heavy calculation are presented.

4.3.3 The Force

The total force consists of the force exerted by the pump plus the force exerted by the repump:

$$\langle F \rangle = \langle F^{(p)} \rangle + \langle F^{(r)} \rangle \ . \tag{4.55}$$

According to Eqs. (4.26) and (4.28) the force of the pump is given by

$$\langle F^{(p)} \rangle = i\hbar k \Omega_p \times Tr \left[\left(\hat{A}^{(p)}_{+1} \right)^\dagger \rho^{st}_{rot} - \left(\hat{A}^{(p)}_{-1} \right)^\dagger \rho^{st}_{rot} \right] + h.c. \tag{4.56}$$

and a similar expression can be found for $\langle F^{(r)} \rangle$. This operation will single out the optical coherences with $m_{F'} = m_F \pm 1$ of the density matrix. Due to the minus sign in the $h.c.$ and the overall i, just the imaginary part will be selected.

In Fig. 4.13 the total force is shown for $\delta = -\Gamma$ and $\delta = 0$. The purple dot-dashed and blue dashed lines show the contributions of the pump and repump laser respectively. It can be seen that the force of the repump laser is negligible for all velocities. This was to be expected since it is tuned to resonance. The total force is largely dominated by the force of the pump laser. For very low velocities $kv \ll \Gamma$, the sub-Doppler feature typical for a multi-level atom in a $\sigma^+ - \sigma^-$ laser configuration can clearly be seen. Note that for $\delta = 0$, and in fact for all $\delta \geq 0$, the slope of the sub-Doppler force is positive and therefore is a heating force.

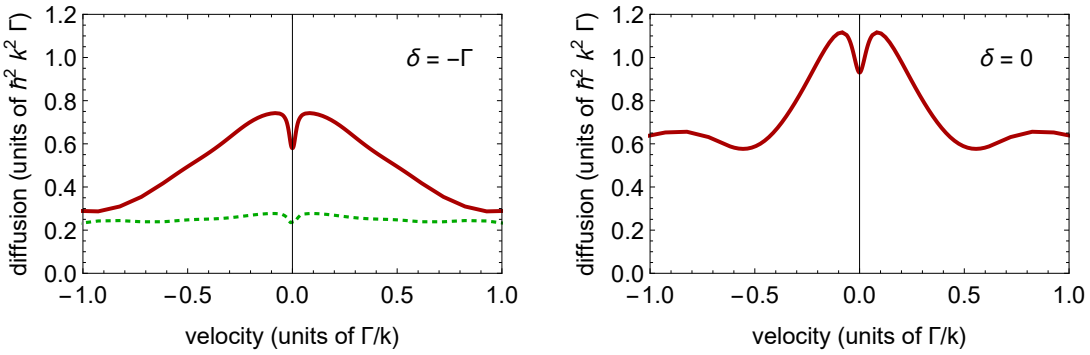

Figure 4.14: The diffusion coefficient felt by a ^{7}Li atom in a $\sigma^+ - \sigma^-$ laser configuration for $\delta = -\Gamma$ (left) and $\delta = 0$ (right) (red solid). Here, as in Fig. 4.13, $\Omega_p = 0.26\ \Gamma$ and $\Omega_r = 0.4\ \Gamma$. For comparison, the diffusion coefficient for the $J_g = 1 \to J_e = 2$ transition from Fig. 4.10 is shown green dotted in the left plot.

4.3.4 The Diffusion Coefficient

The diffusion coefficient has two contributions. One comes from the coupling to the vacuum of the quantized electromagnetic field and reflects the fluctuations in spontaneous emission. Up to a constant, it is the sum of all 16 excited state populations:

$$D_{vac} = \frac{1}{2}\hbar^2 k^2 \Gamma \times \sum_{F'=0}^{3} \sum_{m_{F'}=-F'}^{F'} \rho^{st}_{rot}\left(F', m_{F'}; F', m_{F'}\right). \tag{4.57}$$

The second contribution is due to the fluctuations in the force exerted by the lasers. It is given by the integral of the two-time average as in Eq. (4.30). As mentioned there, the key to doing this computation is the QRT and recognizing the raising and lowering operator pairs that represent physical processes.

The result of the computation is shown in Fig. 4.14 for $\delta = -\Gamma$ and $\delta = 0$. Like the force, the diffusion coefficient also has sub-Doppler features for $kv \ll \Gamma$.

4.3.5 The Temperature

Before calculating the temperature we must decide which procedure to use. If $v_D < v_c$, sub-Doppler cooling starts working and the temperature is determined by the steep slope of the force and the constant value of the diffusion coefficient around $v = 0$. If, on the other hand, $v_D > v_c$ the entire structure of the force and the diffusion coefficient must be used. For ^{7}Li one finds $\omega_r \approx 0.0103\ \Gamma$ and therefore, following Eq. (4.40),

$$\frac{k v_D}{\Gamma} \approx 0.14\,. \tag{4.58}$$

By looking at Figs. 4.13 and 4.14 and especially the insets of Fig. 4.13 we conclude $v_D > v_c$. Alternatively, condition (4.40) is not fulfilled. One must resolve to the

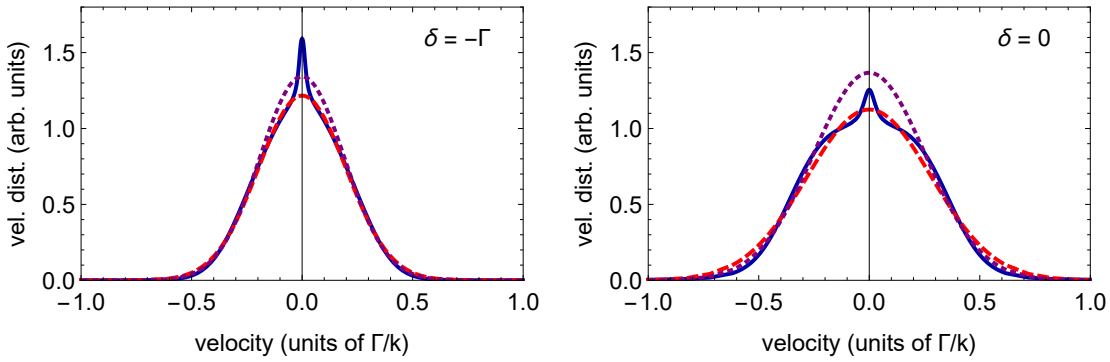

Figure 4.15: The velocity distribution $W(v)$ is shown as a function of the atomic velocity as a blue solid line for $\delta = -\Gamma$ (left) and $\delta = 0$ (right). The dashed and dotted lines are Gaussian fits to $W(v)$ without the points for $|v| < 0.04\ \Gamma/k$ and $|v| < 0.2\ \Gamma/k$ respectively.

second (more complicated) procedure.

Plugging $F(v)$ and $D(v)$ into Eq. (2.36) and solving the integral numerically one obtains the distribution $W(v)$ shown in Fig. 4.15. As can be seen the distributions are non-Gaussian. In addition to the non-Gaussianity appearing for $\delta \to 0$, which was seen earlier, a sharp peak is produced around $v = 0$ for all values of δ. This is due to the sub-Doppler features in the force and the diffusion coefficient. Following our discussion above the sub-Doppler mechanism is inefficient in the case of lithium and the appearance of these features can be attributed to the simplified 1D approach. To extract meaningful information from the theory, we thus ignore the region $|v| < v_{cut}$ and fit the remaining distribution to a Gaussian for different values of v_{cut}. Two examples are shown in Fig. 4.15. The results of the computations are shown in Fig. 4.16, where they are compared to the two-level atom and the $J_g = 1 \to J_e = 2$ transition. Looking at the figure, a few new and interesting features are seen for ^{7}Li. First, the minimal temperature is a factor ~ 2 higher than the Doppler limit. The extra heating discovered in the $J_g = 1 \to J_e = 2$ transition is even more exemplified here. But more interestingly, a steady state temperature is predicted for $\delta = 0$.

The width of the orange region is an indication of the non-Gaussianity of the velocity distribution. For large negative detuning the variation from a Gaussian is small but as we approach resonance it grows, except for one minor (surprising) decrease at $\delta \approx -0.1\ \Gamma$. For positive detuning ($\delta > 0$) the distribution splits into a double peaked function due to the positive slope in the force. This makes the theory very hard to trust and is therefore represented in Fig. 4.16 by a dotted instead of a solid boundary.

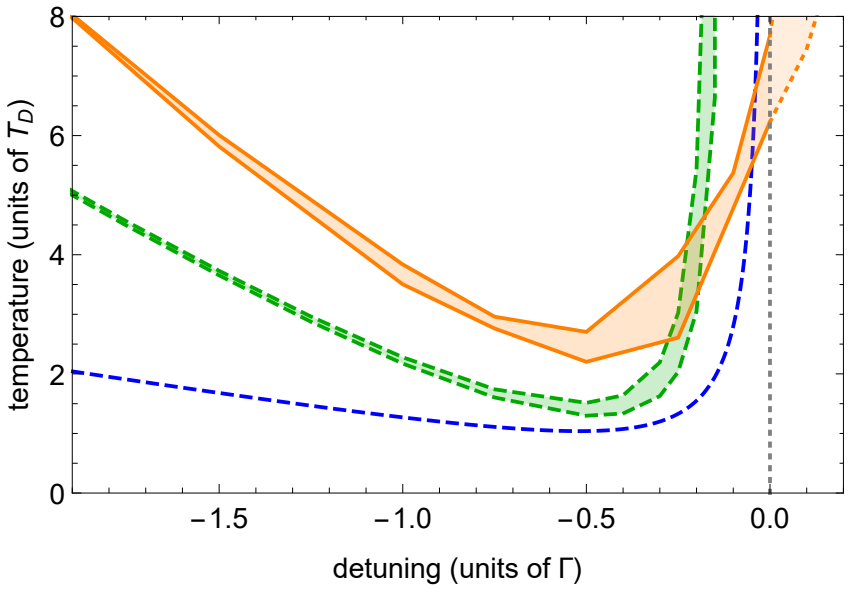

Figure 4.16: A plot of the temperature as a function of detuning for ^{7}Li (orange region, solid boundary). For comparison the simple two-level prediction (blue dashed) and the $J_g = 1 \rightarrow J_e = 2$ transition calculation from Fig. 4.11 (green region, dashed boundary) are shown.

4.3.6 Interpretation

The full ^{7}Li theory shows that cooling at resonance is possible, which is in agreement with the experiment.

A first way to understand this surprising result is to look at the level diagram in Fig. 3.1. Since the $|F = 2\rangle \rightarrow |F' = 3\rangle$ transition is the strongest the pump detuning is measured relative to it. So when $\delta = 0$ this main transition cannot contribute to cooling. The remaining two transitions though, namely $|F = 2\rangle \rightarrow |F' = 2, 1\rangle$, are red detuned and therefore do support cooling. This effect is only possible because the hyper-fine structure of the excited state is inverted which, as mentioned, is an almost unique feature of ^{7}Li.

Moreover, the sub-Doppler feature of the force at $\delta = 0$ (see Fig. 4.13), which is caused by the $\sigma^+ - \sigma^-$ laser configuration, has a positive slope. This is the opposite of friction. It is heating. But since $v_D > v_c$ the sub-Doppler mechanism fails to work. This heating force is not felt by the atoms because the relevant velocities are not accessible. What the atoms do feel is the cooling force (negative slope) which is present for higher velocities due to the red detuned excited states $|F' = 2, 1\rangle$. Because of the sub-Doppler feature, the force must cross the v-axis at a finite value. This causes the negative slope in the Doppler region to be steeper than it would be in the absence of sub-Doppler features. It is therefore apparent that the failure of sub-Doppler cooling increases the effectiveness of Doppler cooling in ^{7}Li.

It is thus the combination of the closely spaced and inverted hyper-fine structure,

the special polarization configuration and the failure of sub-Doppler cooling that allows a steady state temperature at resonance.

Chapter 5

Comparison: Theory VS Experiment

In this section the experimental data from Sec. 3.3.1 and the full multi-level theory derived in Sec. 4.3 are compared. This comparison is illustrated in Fig. 3.5, where the experimental data is shown as black points while the theory is shown as an orange region. The parameters used for the numerical calculations, namely $\Omega_p = 0.26\ \Gamma$, $\Omega_r = 0.4\ \Gamma$ and $\delta_r = 0$ while $\delta_p = \delta$ is varied, are derived directly from the experiment. We stress that there is no fitting parameter in the orange region of Fig. 3.5. The lower and upper boundary of the region correspond to the minimal and maximal dismissed velocity range (see Fig. 4.15).

In the region $\delta < -\Gamma$ the agreement is very satisfactory. Not only are the experimental points, up to experimental errors, within the numerical calculation, the calculated region itself is quite narrow in this regime. This is due to the fact that the non-Gaussianity is less exemplified for $\delta < -\Gamma$.

The absolute minimum is on the order of $\sim 2\ T_D$. Both the experiment and the theory agree with this although they are obtained for slightly different detunings.

Around resonance ($\delta = 0$) the distribution becomes much more non-Gaussian. We therefore do not expect perfect agreement. As discussed in Sec. 4.3.5, this is attributed to the 1D character of the calculations since it is not observed in the experiment. The calculations do, though, show a steady state temperature and thus explain the nature of cooling at resonance. On the one hand, we need a closely spaced, inverted hyper-fine structure and a $\sigma^+ - \sigma^-$ laser configuration. On the other hand, an atomic species for which regular sub-Doppler cooling fails must be used. It is quite likely that, as of today, ^{7}Li is unique in featuring all necessary conditions. But since new and more exotic atoms are constantly being introduced to laser cooling [34–36] this might find application beyond ^{7}Li in the future.

Chapter 6

Monte-Carlo Simulations

6.1 Outline and Purpose of the Simulations

In Sec. 4.3.5 the velocity distribution $W(v)$ for the ^{7}Li atom was found by numerically solving the FP equation. The result is shown in Fig. 4.15. Although it is highly non-Gaussian, the temperature is extracted by fitting $W(v)$ to a Gaussian. This is justified by the experiment whose results are discussed in Sec. 3.3.1 and in which perfect Gaussian distributions are observed. The non-Gaussianity of the theory is attributed to the fact that the model is 1D whereas the (real) experiment is 3D. In this section a 3D Monte-Carlo simulation is setup and its results discussed.

Simulating OBE by means of Monte-Carlo is not trivial. In fact, a regular (classical) Monte-Carlo is not sufficient. To get perfect agreement, a full Monte-Carlo wave function (or quantum Monte-Carlo) simulation must be conducted [37–39]. Such a scheme would also take coherent two-photon processes, which are necessary for sub-Doppler cooling, into account. But since we know that sub-Doppler cooling does not work for ^{7}Li this is not necessary in our case. Instead we build a semi-classical, simplified version of MC simulations (sMC). As in the numerical calculations of Sec. 4.3, the 24 Zeeman sublevels, the two laser frequencies and their polalizations are taken into account. In addition, the 3D character of the experiment is respected: the velocity is a vector with three components and there are a total of six laser beams (one from each direction). The simplification is that only one photon processes, namely absorption and spontaneous emission, are considered and that we also know the state of the atom (no wave function). Therefore, if this simplified simulation reproduces the experimental results, we will have verified the fact that sub-Doppler cooling is irrelevant for ^{7}Li. If, on the other hand, the simulation does not match the experiment, we will conclude that coherent two-photon processes are not at all negligible.

6.2 Algorithm

The sequence of the sMC simulation is described here for a single atom. Obviously it must be repeated a large number of times. The velocity distribution, and therefore $\langle v^2 \rangle$, is obtained by averaging over all realizations.

After initialization, the sequence consists of two consecutive steps: (1) absorption and (2) spontaneous emission. While these steps are carried out in a loop we constantly have to update the internal state of the atom and the three velocity components. (1) Depending on which ground state the atom is in, it will absorb a photon out of either the pump or the repump laser and depending on its velocity components, there is a different probability to absorb a photon coming from the six different directions. In addition the fact that photons arriving from opposite directions have opposite polarization must also be respected. So the total number of possible events for an atom in the ground state $|F, m_F\rangle$ is

$$\text{number of excited states} \times \text{number of lasers} = 16 \times 6 = 96 \tag{6.1}$$

and the probability for each event is given by

$$P = \beta \times \left| C_{(F', m_{F'}; F, m_F)} \right|^2 \times \frac{2\,(\Omega/\Gamma)^2}{4\,(\delta/\Gamma)^2 + 1}\,, \tag{6.2}$$

where $|F', m_{F'}\rangle$ is the excited state reached. The $\Omega = \Omega_{p,r}$ and $\delta = \delta_{p,r} - \Delta_{F'} - \vec{k} \cdot \vec{v}$ in Eq. (6.2) refer to both the pump and the repump and must be chosen according to the $|F\rangle$ of the initial state. The factor β takes the value 1 if the transition is allowed ($m_{F'} = m_F + q$ and $\Delta F = 0, 1$) and 0 if it is forbidden. Hence, for most of the 96 possible events the probability is $P = 0$. (2) For the spontaneous emission, since it is of random nature, a random direction for the velocity is chosen. The ground state into which the atom decays is independent of this direction and is determined by the ratio of the Clebsch-Gordan coefficients.

The sequence for a single atom is as follows:

1. The atom is initialized randomly in one of the ground states and at a velocity according to a Maxwell-Boltzmann distribution at $T = 50\ T_D$.

2. Absorption:

   (a) Calculate the 96 probabilities [Eq. (6.2)] and choose the occuring absorption event by generating a random number and comparing it to the probabilities.

   (b) Update the internal state and the velocity.

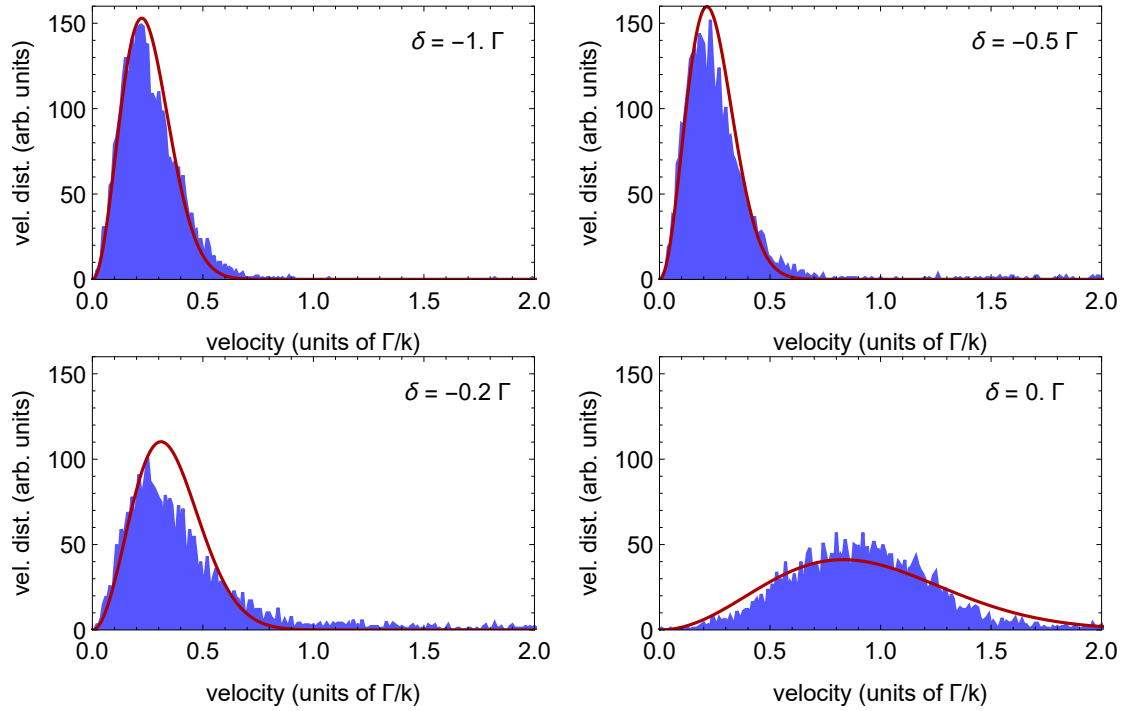

Figure 6.1: Histogram of the three-dimensional velocity distribution for different values of the detuning. It is fitted to a Maxwell-Boltzmann distribution from which the temperature may be extracted.

3. Spontaneous emission:

   (a) Generate three random numbers and normalize them to the recoil velocity. Update the velocity.

   (b) Respecting the Clebsch-Gordan coefficients, find the ground state to decay into and update the internal state.

4. Repeat steps 2-3 many times.

6.3 Results

After a large number of realizations a histogram of the absolute value of the final velocity is made and fitted to a 3D Maxwell Boltzmann distribution given by

$$W(v) = \left(\frac{m}{2\pi k_B T}\right)^{3/2} 4\pi v^2 \exp\left[-\frac{m}{2k_B T} v^2\right] , \tag{6.3}$$

where the only fitting parameter is the temperature T. A few examples are shown in Fig. 6.1. Also here, the phenomenon of non-Maxwell-Boltzmann (3D equivalent to non-Gaussian) distributions is seen for small detunings, although the effect is much less exhibited. For values $\delta \lesssim -0.5$ though, regular distributions are obtained in agreement with the experiment.

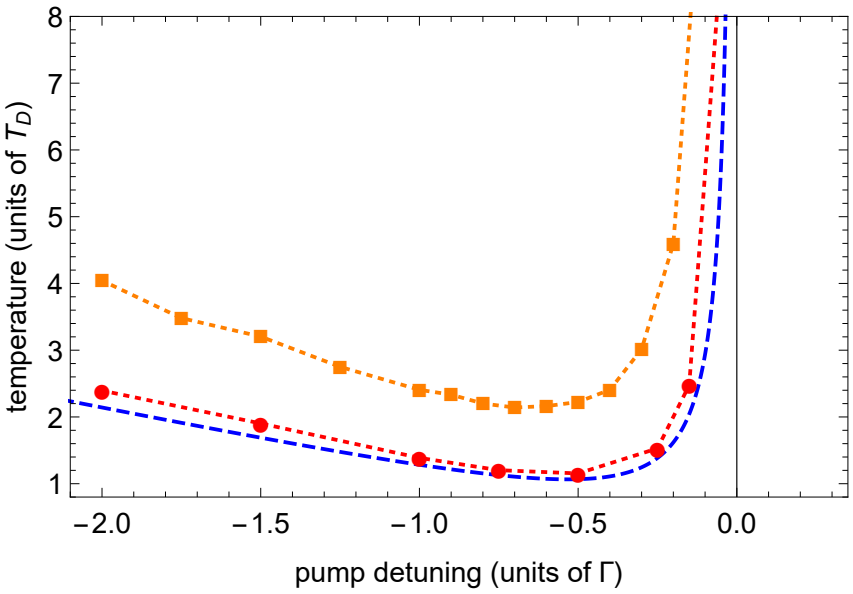

Figure 6.2: Comparison of the results of a semi-classical, multi-level atom, three-dimensional Monte-Carlo simulation to the analytic solution of a two-level atom (blue, dashed). Each point of the simulation is an average over 4000 realizations. In each realization 2500 steps were made (see text). The red dots are obtained when using random laser light polarization. In the $\sigma^+ - \sigma^-$ configuration the orange squares are obtained. The dotted lines are to guide the eye. These results are obtained for small laser intensities so they reflect the minimal temperature.

After extracting the temperature by fitting, it is plotted as a function of the detuning in Fig. 6.2 and compared to the analytical solution [Eq. (2.33)] of the two-level atom. The sMC simulation is run twice. Once for $\sigma^+ - \sigma^-$ polarization and once, for verifying the results, for random polarization. The random polarization simulation (red dots in Fig. 6.2) almost fully recovers the anlytical solution. The minor deviations are due to the multi-level structure of ^{7}Li, the 3D nature of the simulation and finite size effects. For a $\sigma^+ - \sigma^-$ polarization configuration the simulation (orange squares in Fig. 6.2) is a factor of ~ 2 larger. This points to the extra heating, due to the enlarged step size Δp, as pointed out in Sec. 4.2.2. But besides this factor of ~ 2 the behavior of the simulation is comparable to the two-level theory. The main difference is that the simulation shows a steady state temperature of $T \approx 33\ T_D$ at $\delta = 0$. This is an improvement with respect to the random polarization simulation and the analytical two-level theory, but still a factor of ~ 10 above the experiment. Also for large negative detunings no agreement between the simulation and the experiment is found. The $\sigma^+ - \sigma^-$ simulation can give hand waving arguments for the possibility of laser cooling at resonance, but can in no way predict the experimental results. We thus conclude that coherent two-photon processes are very important, not only close to resonance, where this result could have been anticipated, but also for larger detunings, where the usual assumption

is that coherent processes play a negligible role. Thus the sMC simulations are instructive and emphasize the role of coherent processes in the whole range of laser detunings.

Chapter 7

Conclusion

The experimental discovery and theoretical explanation of laser cooling in an unexpected regime is described. Not only do ^{7}Li atoms cooled on the D_2-line remain at a low temperature when the detuning approaches resonance from below, the phenomenon persists at resonance and even for slightly blue-detuned laser light. This stands in direct contradiction with the standard two-level Doppler theory which also fails to predict the experimental results at larger detuning. In order to verify these measurements it was necessary to carefully prepare the setup and acquire a lot of data, allowing accurate data analyses.

In the theoretical part of this work we first introduce Zeeman degeneracy and a $\sigma^+ - \sigma^-$ polarization configuration. This causes an increased diffusion coefficient on the one hand, and, if the Doppler temperature is low enough, a much stronger friction coefficient on the other hand. In the case of ^{7}Li though, the Doppler temperature is not low enough and only the heating remains, partially explaining the higher temperatures for larger detuning. In the second step the hyper-fine splitting and, in particular, the inverted hyper-fine structure of the excited state is considered. This leads to a full understanding of laser cooling at resonance. The ingredients are:

1. closely spaced and inverted hyper-fine structure of the excited state
2. $\sigma^+ - \sigma^-$ laser configuration[1]
3. failure of sub-Doppler cooling

Good agreement between the experiment and theory is shown. The remaining discrepancy is attributed to the 1D character of the theory.

In addition, using a simplified MC approach, the crucial role of coherent two-photon processes is demonstrated. For future research, it would be desirable to build

[1] Another laser setup that leads to sub-Doppler temperatures is lin$\perp$lin [23]. Also in this case there is a capture velocity which, in the case of ^{7}Li, is below the Doppler velocity. The conclusions drawn here for $\sigma^+ - \sigma^-$ most likely also apply for lin$\perp$lin, although we have not analyzed this system in detail.

a full MC wave function simulation. Such an approach should be able to describe the experiment without discrepancies.

Finally we mention a possible application for cooling at resonance. The big advantage is naturally the combination of efficient cooling and high photon scattering rate. Therefore, accurate atom counting experiments with single-atom resolution [40] could benefit largely from this combination.

Bibliography

[1] Y. Yudkin and L. Khaykovich. "Laser Cooling at Resonance". In: *Phys. Rev. A* 97 (2018), p. 053403.

[2] C. Cohen-Tannoudji and D. Guery-Odelin. *Advances in Atomic Physics: An Overview*. World Scientific, 2011.

[3] T. W. Haensch and A. L. Schawlow. "Cooling of gases by laser radiation". In: *Opt. Com.* 13 (1975), p. 68.

[4] D. Wineland and H. Dehmelt. In: *Bulletin of the APS* 20 (1975), p. 637.

[5] J. P. Gordon and A. Ashkin. "Motion of atoms in a radiation trap". In: *Phy. Rev. A* 21 (1980), p. 1606.

[6] S. Chu, L. Hollberg, J. E. Bjorkholm, A. Cable, and A. Ashkin. "Three-dimendional viscous confinement and cooling of atoms by resonance radiation pressure". In: *Phys. Rev. Lett.* 55 (1985), p. 48.

[7] P. D. Lett, R. N. Watts, C. I. Westbrook, W. D. Phillips, P. L. Gould, and H. J. Metcalf. "Observation of Atoms Laser Cooled below the Doppler Limit". In: *Phys. Rev. Lett.* 61 (1988), p. 169.

[8] M. H. Anderson, J. R. Ensher, M. R. Matthews, C. E. Wieman, and E. A. Cornell. "Observation of Bose-Einstein Condensation in a Dilute Atomic Vapor". In: *Science* 269 (1995), p. 198.

[9] K. B. Davis, M.-O. Mewes, M. R. Andrews, N. J. van Druten, D. S. Durfee, D. M. Kurn, and W. Ketterle. "Bose-Einstein Condensation in a Gas of Sodium Atoms". In: *Phys. Rev. Lett.* 75 (1995), p. 3969.

[10] E. Lutz. "Anomalous diffusion and Tsallis statistics in an optical lattice". In: *Phys. Rev. A* 67 (2003), p. 051402.

[11] P. Douglas, S. Bergamini, and F. Renzoni. "Tunable Tsallis Distributions in Dissipative Optical Lattices". In: *Phys. Rev. Lett.* 96 (2006), p. 110601.

[12] Y. Castin, H. Wallis, and J. Dalibard. "Limits of Doppler Cooling". In: *J. Opt. Soc. Am. B* 6 (1989), p. 2046.

[13] C. Cohen-Tannoudji. "Atomic motion in laser light". In: *Fundamental Systems in Quantum Optics, Les Houches session LIII*. Ed. by J. Dalibard, J. M. Raimond, and J. Zinn-Justin. Elsevier Science, Amsterdam, 1992.

[14] C. Cohen-Tannoudji, J. Dupont-Roc, and G. Grynberg. *Atom-Photon Interactions: Basic Processes and Applications*. Wiley Science, 1998.

[15] C. J. Foot. *Atomic Physics*. Oxford University Press, 2005.

[16] J. L. Basdevant and J. Dalibard. *The Quantum Mechanics Solver*. Springer, 2000.

[17] J. Dalibard. "Une breve histoire des atomes froids". In: *Lecture given at College de France*. http://www.phys.ens.fr/ dalibard/index_en.html (unpublished), 2014.

[18] H. J. Metcalf and P. van der Straten. *Laser Cooling and Trapping*. Springer, 1999.

[19] K. Molmer. "Density Matrices and the Quantum Monte-Carlo Method in Quantum Optics". In: *Lectures presented at the Winter School on Quantum Optics, International Centre of Theoretical Physics, Trieste, Italy.* (unpublished), 1994.

[20] H. Nyquist. "Thermal Agitation of Electric Charge in Conductors". In: *Phys. Rev.* 32 (1928), p. 110.

[21] H. B. Callen and T. A. Welton. "Irreversiblity and Generalized Noise". In: *Phys. Rev.* 83 (1951), p. 34.

[22] D. Dreon, L. A. Sidorenkov, C. Bouazza, W. Maineult, J. Dalibard, and S. Nascimbene. "Optical cooling and trapping of highly magnetic atoms: the benefits of a spontaneous spin polarization". In: *J. Phys. B: At. Opt. Phys.* 50 (2017), p. 065005.

[23] J. Dalibard and C. Cohen-Tannoudji. "Laser cooling below the Doppler limit by polarization gradients: simple theoretical models". In: *J. Opt. Soc. Am. B* 6 (1989), p. 2023.

[24] R. Chang, A. L. Hoendervanger, Q. Bouton, Y. Fang, T. Klafka, K. Audo, A. Aspect, C. I. Westbrook, and D. Clement. "Three-dimensional laser cooling at the Doppler limit". In: *Phys. Rev. A* 90 (2014), p. 063407.

[25] J. J. McFerran, L. Yi, S. Mejri, and S. Bize. "Sub-Doppler cooling of fermionic Hg isotopes in a magneto-optical trap". In: *Opt. Lett.* 35 (2010), p. 3078.

[26] N. Gross and L. Khaykovich. "All-optical production of Li-7 Bose-Einstein condensation using Feshbach resonances". In: *Phys. Rev. A* 77 (2008), p. 023604.

[27] U. Schünemann, H. Engler, M. Zielonkowski, M. Weidemüller, and R. Grimm. "Magneto-optic trapping of lithium using semiconductor lasers". In: *Opt. Com.* 158 (1998), p. 263.

[28] N. Gross. "Experimental Study of Universal Three-Body Physics with Ultracold Bosonic Lithium". PhD thesis. Bar-Ilan University, Ramat-Gan, 2011.

[29] C. Cohen-Tannoudji, J. Dupont-Roc, and G. Grynberg. *Photons and Atoms: Introduction to Quantum Electrodynamics*. Wiley Science, 1989.

[30] J. Dalibard, S. Reynaud, and C. Cohen-Tannoudji. "Potentials of a new $\sigma^+ - \sigma^-$ laser configuration for radiative cooling and trapping". In: *J. Phys. B* 17 (1984), p. 4577.

[31] J. W. Dunn. "Stochastic Models of Atom-Photon Dynamics with Applications to Cooling Quantum Gases". PhD thesis. University of Colorado, Boulder, 2007.

[32] M. Lax. In: *Phys. Rev.* 172 (1968), p. 350.

[33] Y. Castin and K. Mølmer. "Atomic momentum diffusion in σ_+-σ_- laser configuration: influence of an internal sublevel structure". In: *J. Phys. B: At. Opt. Phys.* 23 (1990), p. 4101.

[34] A. J. Berglund, J. L. Hanssen, and J. J. McClelland. "Narrowline magneto-optical cooling and trapping of strongly magnetic atoms". In: *Phy. Rev. Lett.* 100 (2008), p. 113002.

[35] M. Lu, N. Q. Burdick, S. H. Youn, and B. Lev. "Strongly dipolar Bose–Einstein condensate of dysprosium". In: *Phy. Rev. Lett.* 107 (2011), p. 190401.

[36] K. Aikawa, A. Frisch, M. Mark, S. Baier, A. Rietzler, R. Grimm, and F. Ferlaino. "Bose–Einstein condensation of erbium". In: *Phy. Rev. Lett.* 108 (2012), p. 210401.

[37] J. Dalibard, Y. Castin, and K. Molmer. "Wave-Function Approach to Dissipative Processes in Quantum Optics". In: *Phys. Rev. Lett.* 68 (1992), p. 580.

[38] R. Dum, P. Zoller, and H. Ritsch. "Monte Carlo simulation of the atomic master equation for spontaneous emission". In: *Phys. Rev. A* 45 (1992), p. 4879.

[39] K. Molmer, Y. Castin, and J. Dalibard. "Monte Carlo wave-function method in quantum optics". In: *J. Opt. Soc. Am. B* 10 (1993), p. 524.

[40] D. B. Hume, I. Stroescu, M Joos, W. Muessel, H. Strobel, and M. K. Oberthaler. "Accurate Atom Counting in Mesoscopic Ensambles". In: *Phys. Rev. Lett.* 111 (2013), p. 253001.

תקציר

המנגנון של קירור דופלר עבור אטום שתי-רמות מבוסס על שימוש בשני קרני לייזר שמתקדמות בכיוונים מנוגדים ותדר מוסך מעט לאדום, אשר יוצרות כיוון מועדף של בליעה, ולכן כוח חיכוך, עבור אטום הנע בתוכם. פליטה ספונטנית, אשר באופן טבעי בא בעקבות כל בליעה, גורמת לאטום לבצע מהלך אקראי בתחום התנע ולכן המהירות עולה באופן דיפוזיבי. כאשר כוח החיכוך (קירור) והדיפוזיה (חימום) נמצאים בשיווי משקל, הצבר האטומי מגיע לטמפרטורת המצב היציב. טמפרטורה זו, שהיא הנושא העיקרי של התזה, תלויה בכמה רחוק מתהודה הלייזר מוסך.

אנו מראים בניסוי כי קירור לייזר של אטומי ליתיום (^{7}Li) על הקו האטומי D_2 אפשרי כאשר אור הלייזר מכוון בדיוק לתהודה עם המעבר האטומי הדומיננטי. מכיוון שזה סותר את התחזית של קירור דופלר (אין כיוון בליעה מועדף ולכן אין כוח קירור), אנו בונים מודל תיאורטי מורכב יותר כדי להסביר את התופעה. התזה מורכבת משני חלקים: אחד ניסיוני ואחד תיאורטי.

בחלק הניסיוני אנו מאמתים את התצפית של קירור בתהודה. זה כולל קביעת תדירות אבסולוטית של הלייזר השואב עם דיוק גבוהה על ידי ניתוח קפדני של הספקטרום הנפלט על ידי האטומים כאשר הם נאורים על ידי הלייזר השואב. בנוסף, יציבות תדר הלייזר הוגדלה ל-$\sim 100\ kHz$ ($\lesssim 0.02\ \Gamma$, כאשר Γ הוא הרוחב של הרמה המעוררת) על ידי נעילת הלייזר דרך הזרם שמפעילה את דיודת הלזירה. מתכונת זו מאפשרת שליטה הרבה יותר מהירה בתדירות מאשר הטכניקה הסטנדרטית שמבוססת על נעילה דרך הפייזו מכיוון שעוקפים את כל הרכיבים המכניים. בסך הכל, השגיאה הניסויית בקביעת התדירות נאמדת $\lesssim 0.05\ \Gamma$. גם השגיאה במדידת הטמפרטורה נעשית קטנה ככל האפשר לשם כך, הטמפרטורה נמדדת קודם כפונקציה של זמן הקירור וטמפרטורת המצב היציב מופקת על ידי התאמה לפונקציה. על ידי הסתכלות על זמן מספיק ארוך אנו יכולים גם לוודא כי האטומים אכן מגיעים למצב יציב בתוך (בדרך כלל) פחות מ-$1\ ms$.

מבחינה איכותית, ניתן להבין את התופעה של קירור בתהודה על ידי יישום נימוקים פשוטים של קירור דופלר למבנה העל-דק של המצב המעורר של ^{7}Li. מאחר והוא צפוף והפוך המעבר הדומיננטי, ביחס אליו נמדד הסכת התדר, הוא הנמוך ביותר באנרגיה, ואילו שאר הרמות המעוררות, שנותרו בהסחה לאדום, נמצאות קרובות מספיק כדי לאכלסם. עם זאת, כדי לבנות תיאוריה כמותית טובה, שהיא הנושא של החלק השני, עלינו לפתור מודל מלא אשר לוקח בחשבון הן את המבנה האטומי של כל 24 התת-רמות והן את קיטוב אור הלייזר ($\sigma^+ - \sigma^-$) אשר מוכתב על ידי המלכודת האופטי-מגנטית. שילוב התכונות הללו בתיאוריה אינו פשוט. לכן, אנו מתחילים על ידי ניתוח של כמה מערכות פשוטות (המעברים $J_g = 0 \to J_e = 1$ ו-$J_g = 1 \to J_e = 2$) ומציגים

את התכונות בזו אחר זו. כך, התופעות הפיזיקליות המופיעות עם כל תכונה מוצגים בצורה מסודרת. בפרט, מצב יסוד מנוון, כמו במקרה של המעבר $J_g = 1 \rightarrow J_e = 2$ ו-7Li, גורם להופעת שני סקלות של מהירות. אחד, שנקרא מהירות דופלר v_D, היא המהירות הטיפוסית שאטום מקבל בקירור דופלר. השני היא המהירות המינימלית כדי שאטום ילכד בקירור תת-דופלר v_c, מנגנון קירור יעיל מאוד הנובע מחוסר איזון בין האוכלוסיות ברמות היסוד. אם $v_D < v_c$ האטום יחווה קירור נוסף זה, אם $v_D > v_c$ קירור תת-דופלר ייכשל. זה ידוע (ניסויית) כי ב-7Li האחרון הוא מקרה וזה גם מאומת (תיאורטית) על ידי ניתוח זהיר של פרופיל הכוח ומקדם הדיפוזיה. כאן אנו מראים, כי העובדה כי מנגנון התת-דופלר נכשל ב-7Li משפר קירור דופלר בתהודה ובנוסף משפיע מאוד על טמפרטורת המצב היציב עבור הסכה גדולה ושלילית.

יתר על כן, באמצעות סימולציות מונטה-קרלו אנו מראים כי תהליכים קוהרנטיים ממלאים תפקיד חשוב בהצגת עקביות בין התיאוריה לבין תוצאות הניסוי.

בקירור בתהודה יש שילוב מושלם של קצב פיזור פוטונים מקסימלי עם תנאיי קירור יעילים. זה יכול להיות מיושם ישירות בניסויים של ספירת אטומים מדויקים עם רזולוציה של אטום יחיד אשר בבירור ייהנו משילוב זה.

עבודה ניסויית-תיאורטית זו התפרסמה לאחרונה ב-Physical Review A והוצגה כ-"הצעת העורך" [1].

עבודה זו נעשתה בהדרכתו של

פרופ' לב חייקוביץ

מן המחלקה לפיסיקה
של אוניברסיטת בר-אילן.

אוניברסיטת בר-אילן

קירור לייזר בתהודה

יעקב יודקין

עבודה זו מוגשת כחלק מהדרישות לשם קבלת תואר מוסמך

במחלקה לפיסיקה של אוניברסיטת בר-אילן

רמת גן תמוז תשע"ח